Journal of
Ceramic Science
and Technology

J. Ceram. Sci. Technol., **11** [1] 44-61 (2020)
DOI: 10.4416/JCST2019-00071
available online at: http://www.ceramic-science.com

Circuit-Board-Integrated Transformers Design and Manufacture

R. Matz[1], T. Rabe[2], J. Töpfer[3], S. Ziesche[*4]

[1]Siemens Corporate Technology, D-81730 Munich, Germany (retired)
[2]Federal Institute for Materials Research and Testing, D-12203 Berlin, Germany
[3]Ernst Abbe University of Applied Sciences, D-07745 Jena, Germany
[4]Fraunhofer Institute for Ceramic Technologies and Systems IKTS, D-01277 Dresden, Germany
received November 5, 2019; received in revised form Januar 7, 2020; accepted Januar 17, 2020

Abstract

Transformers couple two sections of a circuit by electromagnetic induction. They are widely used to either transform alternating voltage levels or to transmit power or signals across galvanic isolation. Both of these functions are essential for the operation of sensors and controllers. Covering all aspects from idea to circuit performance and from design to manufacture, this paper presents the first comprehensive description of the making of miniaturized, rugged, up-to-100 W transformers for embedding into multilayer circuit boards. For circular coils, the well-manageable Ampere-Laplace law is shown to yield reliable designs, predicting correctly the performance of manufactured hardware. This enables fast design without lengthy finite element modelling. In the low-power linear regime, basic relations describe how the device's characteristics evolve from the material properties and device structure. While scattering parameters are useful for the analysis of isolated transformers with their intrinsic parasitics, the interaction with the components of the final circuit and the aspects of power and efficiency are addressed by chain matrixes.

While these design rules are similar for multilayer boards of different material (like epoxy, Teflon, ceramics), the manufacturing of ceramic board transformers is considered here in detail. Low-temperature-cofired ceramic (LTCC) boards being sintered at 900 °C are particularly suited for harsh environments with chemical or thermal stress as frequently found at sensor positions. The transformer performance usually benefits from or even requires an integrated ceramic core of higher permeability, a ferrite, to shape the magnetic flux. Methods to sinter ferrites inside a dielectric ceramic multilayer and to measure their performance are therefore described in detail. As the sintering behaviour of dielectric and magnetic ceramics differs considerably, their simultaneous sintering is challenging. However, the sintering temperatures of the useful MnZn and NiZnCu ferrites can be lowered to that of the dielectric material with only moderate loss of permeability by glass additives. Furthermore, thermal mismatch between materials causes catastrophic failure or at least stress and loss of magnetic performance during cooling to room temperature after sintering. This is avoidable by either adjusting the thermal expansion coefficient of the ferrite or by enclosing the ferrite between stress-releasing separation layers. We present the state of the art in materials development according to the first approach as well as fully functional devices made with the second technique.

Other applications not directly addressed but well related to this work are characterized by low load resistance in relation to the coil resistance of the transformer. Efficient power transmission then requires that technological solutions are applied to achieve the lowest possible resistive loss inside the coils by an enlarged conductor cross-section. As this is particularly challenging for LTCC boards, a technique is discussed to fabricate conductor traces with a thickness larger than their width.

Keywords: Multilayer ceramic technology, LTCC, transformer

I. Introduction

Complex technical systems in industry and infrastructure as e.g. power plants, refineries, smart buildings, autonomous trains and cars or evolving power grids with their distributed functions of generation, transportation, conversion, storage, and consumption rely on continuous condition monitoring for their efficient operation. To this end, numerous rugged sensors, controllers, and drivers are to be embedded to send data upstream ("big data") for processing and alignment with a system model and to receive control signals in reverse direction. Thus, intensive research and development has been undertaken during the last two decades in miniaturized circuits which integrate digital and analog electronics with passive components, mainly capacitors and inductors. The intricacy of magnetic fields and materials, however, has retarded the progress in case of inductive components. Major parameters to be linked in an optimal design are circuit-relevant impedance,

* Corresponding author: steffen.ziesche@ikts.fraunhofer.de

current carrying capacity, and quality factor, i.e. low resistive and eddy current loss. Accordingly, various designs and materials have been employed to address the application-specific key aspects: High frequency, high quality or high inductance.

At high frequency as in wireless communication and microwave circuits, small inductors with nH inductances usually develop sufficient impedance, which is the product of inductance and angular frequency. They are naturally small and can be integrated on Si chips. High self-resonant frequencies and quality factors have been demonstrated using various microelectromechanical techniques [1–3]. Magnetic ceramics or ferrites like Ba hexaferrite amplify the magnetic flux density so that further inductance-size combinations become accessible [4,5]. For energy harvesting, even microtransformers have been realized on-chip with bond wires surrounding a toroidal surface-mounted ferrite core [6].

High-quality inductors are placed off-chip on low-loss insulating substrates like ceramics. Low-temperature-cofired ceramics (LTCC) in particular exhibits cost advantages over thin-film technologies: Holes are mechanically punched into individual ceramic green tapes and filled with Ag paste for vertical interconnects; planar conductor traces are formed by screen printing of Ag paste onto the tape surface; finally, a multitude of tapes is laminated to form a multilayer board which is sintered at a relatively low temperature around 900 °C. To achieve this level below the melting point of Ag, the major constituent of common metallization pastes, various glasses are used as sintering additives in the ceramic tapes. LTCC has a proven record in automotive and aviation owing to its hermeticity and robustness, but also in microwave and wireless applications, where its excellent loss and miniaturization performance are exploited. Embedded inductors can be miniaturized by means of innovative printing methods for narrower conductor lines [7], but this comes at the expense of current-carrying capacity.

High inductance values in the µH range are needed for lower frequencies in power electronics as for example for power converters, lamp ballasts and switched-mode power supplies. Here, the amplification of the magnetic flux by magnetic materials is mandatory and ferrites are preferred, since their magnetic losses are lower than those of magnetic metals at frequencies above a few 100 kHz [8]. For inductor coils inside a printed circuit board (PCB) the simplest approach are magnetic layers attached to both sides of the PCB, e.g. electroplated Ni-Fe [9] or ferrite polymer compound layers [10]. Inversely, the metallic turns of an inductor may also be deposited with insulating dielectric layers on a ferrite substrate [11]. Even larger inductance values of up to several 100 µH have been demonstrated at higher currents by embedding the inductor coil into low-temperature-cofired ferrite (LTCF) multilayer [12–15]. While this technology is easy and yields quite large inductors, it suffers from weak electric isolation and loss of magnetic flux between the turns of the inductor coil.

As the magnetic field lines form closed loops in planes perpendicular to the current in a toroidal-like coil, the ideal technology would be capable of embedding the coil in dielectric insulating material and surrounding this dielectric torus with ferrite material. The traditional approximation uses E-shaped ferrite cores being inserted with their three legs through holes in the circuit board; a ferrite plate attached to the back side closes the magnetic flux [16]. These assembled structures are magnetically effective and easy to fabricate, but unqualified for embedding and miniaturization. To this end, attempts have been made to add magnetic cores to solenoidal inductors by filling blind holes with ferrite nanopowder [17] or cofired ferrite tapes [18]. The absence of ferrite cover layers, however, imposes a high magnetic reluctance outside the board and impairs the effect in these cases. An elegant monolithic version was demonstrated by filling openings in a dielectric ceramic circuit board with Ni-Cu-Zn ferrite paste and cofiring with top and bottom ferrite tapes [19].

Different from a single inductor, the magnetic flux must pass entirely through the two coils of a transformer to constitute magnetic coupling. Depending on the thickness of the circuit board and the desired electrical performance, one of three basic structures may be chosen: The closed core, the dielectric gap, and the ferrite-embedded type. Examples for any of these have appeared in literature, but many are incompatible with usual circuit board technologies. A closed core, as described before, consists of ferrite plates on the board surfaces that are magnetically connected by ferrite filled through holes (vias) [20]. The gap type is similar but omits the magnetic feedthroughs to ease fabrication [10,21–23]. For the embedded transformer, the conductor turns are embedded in a ferrite multilayer. To avoid bypass currents and magnetic flux loss between the turns, dielectric material has to be added around the conductors. This is either achieved by screen printing of dielectric paste [24–6] or by using a modified nonmagnetic ferrite material in the immediate neighbourhood of the conductors [27].

The present article reviews design rules, manufacturing technologies, and performance data of individual as well as magnetically coupled circuit board inductors for power electronic applications up to 100 W. They employ Ni-Cu-Zn and Mn-Zn ferrite multilayers and technologies for their integration into regular extended circuit boards. They have emerged in our laboratories under national cooperation and funding over years of materials and component development. As they provide a route for both, the miniaturization and the regular board integration, they go far beyond the state of the art. Transformer structures suitable for space-saving board integration are discussed in the following section. The balance between structural complexity, as demanded by physical laws, and structural simplicity, as required for reliable technology, is emphasized. To set up a process for the design and the performance forecast being more accurate than generalized analytical equations and less laborious than finite element modelling, we use the Ampere-Laplace law to numerically calculate inductances of these designs in the third section. For the linear regime at least, two-port network parameters then allow the parasitic elements to be included and the transmitted power and efficiency of a transformer to be obtained in a circuit. While these results apply to multi-

layer circuit boards in general, the present technology focus is on transformer integration into ceramic boards for high-temperature applications. To this end, the adaptation of Mn-Zn and Ni-Cu-Zn ferrite sintering and the implementation into cofiring processes are considered in section four. Typically, conductor traces are screen-printed onto green tapes before lamination and firing using mixed bonded silver particle pastes. Resulting conductors exhibit fired thicknesses between 15 and 20 µm and a sheet resistivity below 2 mΩ/sq, which is about 50 % of an ideal copper conductor. The chapter therefore also presents both an effective technology for their power electronic strengthening and the conditions for its reasonable application. The performance of cofired transformers finally demonstrates in Section V the functioning and effectiveness of these new technologies.

II. Device Structures

Conventional transformers for surface mounting on printed circuit boards have comparable extension in the three spatial directions. The task of embedding such components into a flat board, therefore, deals with stretching physics and materials to reduce the vertical extension by an order of magnitude while still keeping sufficient device performance. According to Ampère's law, a current-carrying coil is surrounded by magnetic flux. If the "primary" current is time-dependent, a voltage is induced according to the Faraday-Henry law in any closed "secondary" loop or coil through which a fraction of the primary flux passes. For symmetry reasons, the secondary current acts in the reverse direction on the primary circuit. Under harmonic excitation with angular frequency ω, the voltages in the primary and secondary coils V_p and V_s are superpositions of their own flux and the mutual flux Φ_M due to the other coil

$$V_p = -\frac{d\Phi_p}{dt} = j\omega\Phi_p = j\omega(\Phi_1 + \Phi_M),$$
$$V_s = -\frac{d\Phi_s}{dt} = j\omega\Phi_s = j\omega(\Phi_2 + \Phi_M). \quad (1)$$

If the coils are surrounded by dielectric material, e.g. the printed circuit board indicated in Fig. 1(a), some of the primary flux can leak out between the coils and a fraction only magnetizes the secondary coil. The design goal for a transformer consists in aiming at minimal leakage flux.

Good coupling is traditionally achieved by inserting the three legs of an E-shaped ferrite core into three holes of the board such that the central one is aligned along the common axis of the coils as depicted in Fig. 1(b). Ferrites are ceramic materials containing atomic magnetic dipoles which are aligned by the external magnetic field. The magnetic flux density B is consequently amplified by the material's relative permeability $\mu_r = \mu/\mu_0$ in a similar way as the dielectric displacement field in a capacitor is amplified by the permittivity of the dielectric between the electrodes. The effectivity of a magnetic material like a ferrite, however, relies in at least the same manner on its ability to deform the whole magnetic field. Field lines preferably pass through a material of higher permeability, just as electric currents prefer paths of higher electrical conductivity. Out of this analogy, the magnetic resistance or reluctance of a volume element of length l and cross-section A is defined by

$$R_m = l/(\mu_0\mu_r A) \quad (2)$$

With their relative permeabilities of 100 to 150 Ni-Cu-Zn or Mn-Zn ferrites reduce the reluctance to about 1 %. Hence, when a ferrite plate connects the open ends of the "E" on the back side of the board according to Fig. 1(b), most of the magnetic flux lines are trapped in the two low-reluctance loops. There is no more flux leakage between the coils. However, this traditional solution wastes board area that is occupied by a bulky passive ferrite. For high-temperature applications, it would also be desirable to monolithically integrate the dielectric board ceramics with the magnetic ferrite ceramics, ideally in a single cofiring process.

The E-core structure can in principle be translated into LTCC technology with the aid of ferrite-filled vertical through holes (magnetic vias) in an otherwise dielectric multilayer. It turns out, however, that the fill grade of vias is too low to achieve a substantial magnetic cross-section. One might hence investigate the conditions under which simple ferrite plates attached to the bottom and top surfaces of the board without vertical low-reluctance paths perform sufficiently well; see Fig. 1(c). In thick circuit boards, interior field lines with their short loops will be out of range of the ferrite and flux leakage will still occur to some extent. But the outer field lines are captured by the ferrite. It follows from energy conservation that they are refracted at the interface between the dielectric board and the magnetic material according to [28]

$$\tan(\theta_{board}) = \tan(\theta_{ferrite})/\mu_r. \quad (3)$$

Near-vertical field lines in the board (e.g. $\theta_{board} = 2°$) are forced into an almost right angle ($\theta_{ferrite} = 80°$) if captured by the ferrite ($\mu_r = 150$). Their former oval shape is distorted into a rectangle, so that more flux passes through the secondary coil. Under the simplifying assumption that the magnetic cross-section is constant along the closed magnetic path, this fraction of flux experiences an effective reluctance, which is the sum of the ferrite and the dielectric

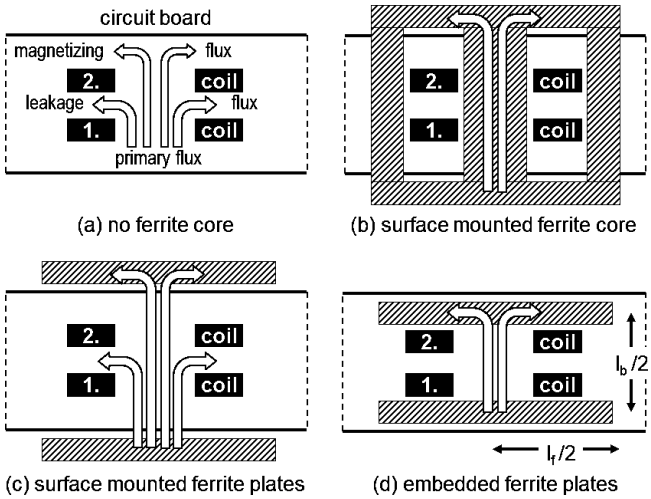

Fig. 1: Cross-sectional views of alternative coil structures and their characteristics of magnetic coupling. Fractions of the closed magnetic path in the dielectric board l_b and in the ferrite l_f are indicated in (d).

gap (i.e. board) reluctances. When l_f and l_b are the magnetic path lengths in the ferrite and board as defined in Fig. 1(d), we find the effective permeability from Eq. (2)

$$\frac{l_f + l_b}{\mu_{eff}} = \frac{l_f}{\mu_r} + l_b \rightarrow \mu_{eff} = \frac{\mu_r\, l}{l + l_b\,(\mu_r - 1)} \approx \frac{l}{l_b} \qquad (4)$$

for large μ_r.

Now the relative gap width $(l_f + l_b)/l_b$ rather than the quality of the ferrite determines the performance. If, for example, the gap amounts to 10 % of the total magnetic path length, the effective permeability is only about 10. This will no longer suffice to concentrate the flux into good magnetic coupling.

Interestingly, as indicated by Fig. 1(d), embedded ferrite plates eliminate most of these drawbacks: They provide additional surface area for surface-mounted devices while keeping the fabrication of the board without vertical ferrite core as simple as possible. The embedding technology on the other hand minimizes the dielectric gap l_b and the loss of magnetic flux through this gap as in Fig. 1(c). Consequently, both the magnetic coupling between the coils and the effective permeability according to Eq. (4) are improved. It will be shown below that these benefits become real for technically relevant dielectric gaps.

III. Design Rules

(1) Magnetic flux

A method is needed to calculate the fluxes of Eq. (1). Finite element modelling usually delivers the electromagnetic fields accurately that govern the device's circuit behavior. However, our analytical model below will permit a much higher throughput of design variations in a standard office software environment and will therefore give a fast answer to the question of feasibility. It takes into account magnetic and capacitive coupling as well as magnetic and resistive losses.

The current in a conductor of finite width w shall be approximated by a narrow current filament in the center of the conductor. Ampère-Laplace's law then yields the flux density vector

$$B = \frac{\mu_0\, I}{4\pi} \oint \frac{u_t \times u_d}{d^2}\, dl \qquad (5)$$

at any point in free space as an integral along the closed filament, where d is the distance between the section dl of the filament and the position at which the field is calculated. u_d is the associated unit vector and u_t is the unit vector tangential to the filament. For a planar circular current filament of radius R, the normal component of B at distance r from the axis and distance z from the filament plane simplifies t

$$B_z(r,z,I) = \frac{\mu_0\, I}{2\pi} \int_0^{\pi} \frac{(R - r\cos\varphi)\, R\, d\varphi}{(R^2 + r^2 + z^2 - 2Rr\cos\varphi)^{3/2}} \qquad (6)$$

The adaptation of this relation to a non-circular, oval conductor turns will be discussed below in conjunction with an actual design example. Now, considering two turns m, n of an inductor coil, the flux through turn n on plane $z = z_n$ due to the current in turn m on plane $z = z_m$ is determined by integration of Eq. (6) over the area within the inner conductor edge of turn n.

$$\Phi_{mn} = 2\pi \int_0^{R_n - w_n/2} B_z(r, z = z_n - z_m, I)\, r\, dr = L_{mn} \cdot I \qquad (7)$$

Thus we also define the mutual inductance element L_{mn}. A singularity is encountered in the integrand of Eq. (6) for r = R and z = 0, i.e. on the current filament. Therefore, our procedure takes into account only the flux, which is outside of conductors. For a single conductor turn, Eq. (7) yields a self-inductance L_{11} as shown by Fig. 2 in good agreement with the traditional result [29]

$$L = \mu_0 R \ln(2R/w) \qquad (8)$$

for a single loop of wire having a loop diameter 2R and wire diameter w.

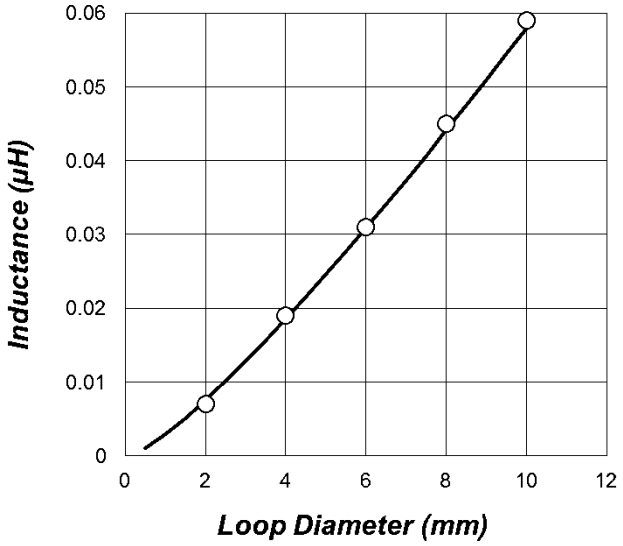

Fig. 2: Congruence of inductances of a circular wire loop with 0.2 mm wire diameter (line) and its approximation by a flat conductor trace of 0.2 mm width (dots) as calculated with (8) and (7), respectively.

The primary and secondary coils of a transformer may have N_1 and N_2 turns, respectively. The transformer as a whole has N_1+N_2 turns, i.e. the Φ_{mn} matrix has rank $N_1 + N_2$. The self and mutual fluxes for use in Eq. (1) are obtained by calculating at first all matrix elements L_{mn}. The self-flux $\Phi(m)$ through any turn m of the primary coil is the sum of flux contributions by all primary turns

$$\Phi(m) = I_1 \sum_{n=1}^{N_1} L_{mn} \approx \Phi_1 \text{ for } 1 \le m \le N_1 \qquad (9)$$

This flux will be similar in all primary turns, for which reason we refer to it as the primary flux Φ_1. Due to the mutual inductive interaction between all turns, the primary self-inductance is defined by

$$L_1 = \sum_{m=1}^{N_1} \sum_{n=1}^{N_1} L_{mn} \approx \frac{N_1 \Phi_1}{I_1} \qquad (10)$$

Similarly, the secondary self-inductance and the mutual inductance are

$$L_1 = \sum_{m=N_1+1}^{N_1+N_2} \sum_{n=N_1+1}^{N_1+N_2} L_{mn} \approx \frac{N_2 \Phi_2}{I_2} \qquad (11)$$

and

$$\begin{aligned} M &= \sum_{m=1}^{N_1} \sum_{n=N_1+1}^{N_1+N_2} L_{mn} \\ &= \sum_{m=N_1+1}^{N_1+N_2} \sum_{n=1}^{N_1} L_{mn}. \end{aligned} \qquad (12)$$

(2) Small and large signal behavior

While the inductances are defined by design, the primary and secondary currents I_1 and I_2 depend on the actual circuit environment. Relating the fluxes of Eq. (1) with the generating currents yields the definition of the impedance matrix Z by

$$\begin{pmatrix} V_1 \\ V_2 \end{pmatrix} = j\omega \begin{pmatrix} L_1 & M \\ M & L_2 \end{pmatrix} \cdot \begin{pmatrix} I_1 \\ I_2 \end{pmatrix} = Z \cdot \begin{pmatrix} I_1 \\ V_2 \end{pmatrix}. \qquad (13)$$

Each primary and secondary main (total) inductance L is the sum of leakage inductance L_L and magnetizing inductance L_M which affects the power transmission of the transformer [30]. The magnetizing inductances are related to the ratio of tums by

$$L_{M1}/L_{M2} = N_1^2/N_2^2 = 1/N_{12}^2. \qquad (14)$$

Their product defines the mutual inductance M and the coupling coefficient k through

$$M^2 = L_{M1} L_{M2} = k^k L_1 L_2. \qquad (15)$$

Small signal data are usually collected by a two-port network analysis of scattering parameters for an initial proof of design. It is therefore useful to express scattering parameters by the impedance matrix elements [31]. The insertion loss S_{21} is found to exhibit three characteristic frequency regimes given by

$$|S_{21}| = \begin{cases} \frac{2N_{21}\omega L_{M1}}{Z_0} \; for\; \omega \le \frac{Z_0}{L_{M1}} \frac{k}{N_{21}{}^2+1} \\ \frac{2k}{N_{21}+1/N_{21}} \; for\; \frac{Z_0}{L_{M1}} \frac{k}{N_{21}{}^2+1} < \omega < \frac{Z_0}{L_{M1}} \frac{k(N_{21}{}^2+1)}{(1-k^2)N_{21}{}^2} \\ \frac{Z_0}{\omega L_{M1}} \cdot \frac{2k^2}{N_{21}(1-k^2)} \; for\; \omega \ge \frac{Z_0}{L_{M1}} \frac{k(N_{21}{}^2+1)}{(1-k^2)N_{21}{}^2} \end{cases} \qquad (16)$$

Magnetizing inductances and coupling coefficient of a manufactured device are therefore obtained by fitting these relations to the measured insertion loss [30].

A refined calculation must include distributed parasitic effects like capacitive coupling between conductors, resistive loss inside conductors and magnetic loss inside the ferrite core. Despite some arbitrariness in mapping distributed to lumped elements, the approach indicated by Fig. 3 has proven useful. It should be read as a combination rule of transmission and admittance matrixes of the individual elements.

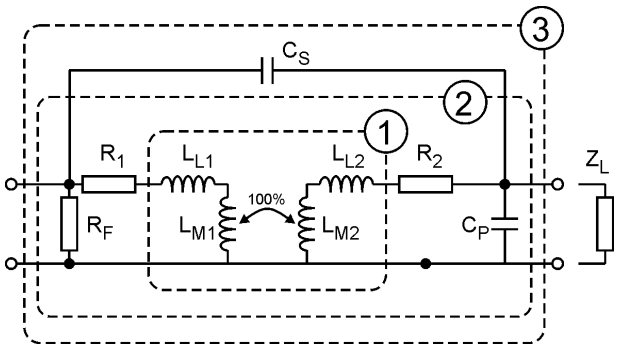

Fig. 3: Equivalent circuit of a transformer with three levels of detail. The finite inductive coupling k is represented on the inner minimum level 1 by leakage inductances L_{L1}, L_{L2} and perfectly coupled magnetizing inductances L_{M1}, L_{M2}. Resistive losses R_1, R_2 of the coils, magnetic losses R_F of the ferrite core and the capacitive coupling C_P inside the coils are added on level 2. The capacitive coupling C_S between the coils is finally accounted for on level 3.

Starting on level 2, the ferrite loss R_F, the primary conductor loss R_1, the secondary conductor loss R_2 and the intra-coil capacitance C_P, acting parallel to the load, form a sequence of transmission (or ABCD) matrixes. As indicated, they enclose the transmission matrix of the bare transformer "T", derived from its impedance matrix in Eq. (13) [31], to yield an intermediate transmission matrix

$$\begin{aligned} &ABCD(R_F, R_1, T, R_2, C_P) \\ &= \begin{pmatrix} 1 & 0 \\ 1/R_F & 1 \end{pmatrix} \cdot \begin{pmatrix} 1 & R_1 \\ 0 & 1 \end{pmatrix} \\ &\begin{pmatrix} L_1/M & j\omega\,(L_1L_2/M - M) \\ 1/j\omega M & L_2/M \end{pmatrix} \\ &\begin{pmatrix} 1 & R_2 \\ 0 & 1 \end{pmatrix} \cdot \begin{pmatrix} 1 & 0 \\ j\omega\, C_P & 1 \end{pmatrix} \end{aligned} \qquad (17)$$

The inter-coil capacitance C_S provides a power transmission path parallel to the transformer in series with the load. Consequently, converting the above $ABCD(R_F,R_1,T,R_2,C_P)$ into its admittance equivalent and adding the admittance representation of C_S yields the admittance matrix of the complete transformer described by level 3

$$Y_3 = Y(R_F, R_1, T, R_2, C_P) + j\omega\, C_S \begin{pmatrix} 1 & -1 \\ -1 & 1 \end{pmatrix} \qquad (18)$$

Despite the simplicity of the matrixes involved, a successive numerical evaluation of Eqs. (17) and (18) is more practical than deriving closed analytical expressions.

The primary and secondary electrical power at the transformer, when combined with a load impedance Z_L, is illustrated best by conversion of Y_3 into its transmission representation $ABCD_3$ so that

$$\begin{pmatrix} V_1 \\ I_1 \end{pmatrix} = \begin{pmatrix} A_3 & B_3 \\ C_3 & D_3 \end{pmatrix} \cdot \begin{pmatrix} V_2 \\ I_2 \end{pmatrix}. \qquad (19)$$

From $V_2 = Z_L \cdot I_2$ we find

$$\begin{aligned} I_1 &= \frac{C_3Z_L + D_3}{A_3Z_L + B_3} V_1; \\ I_2 &= \frac{1}{A_3Z_L + B_3} V_1; \\ V_2 &= \frac{Z_L}{A_3Z_L + B_3} V_1. \end{aligned} \qquad (20)$$

Primary power, secondary power and efficiency are consequently

$$P_1 = \mathrm{Re}(V_1 I_1^*)/2; \quad P_2 = \mathrm{Re}(V_2 I_2^*)/2; \quad \eta = P_2/P_1 \qquad (21)$$

The model or set of design rules, as expressed by Eqs. (4) to (21), delivers a valuable operational forecast about stress on materials and about device performance on circuit level. The required materials-related input quantities can be determined in advance by measurement or from data sheets. Measurements reveal for example the amplitude permeability and the loss of a ferrite core, as will be discussed in detail in Section IV (1) below. Parasitic capacitances are to be estimated by the area and vertical separation of the transformer turns. Conductor losses result from the geometry of the coils and the specific resistivity of the conductor material employed.

(3) Design examples

Although the design rules apply to any circuit board technology, three transformer examples based on LTCC technology will be considered in detail below. Fig. 4 shows their cross-sectional designs. The first one, shown in Fig. 4(a), has oval conductor traces. It minimizes technological difficulty by having separately sintered ferrite plates attached to a conventional dielectric multilayer board. As the plates can be exchanged nondestructively, various commercial and specifically manufactured ferrites can be compared on a single embedded coil system for test purposes. Eq. (6) can be adapted to the oval shape by introducing an effective circular design with identical conductor widths and spacings. As the 9 mm length of the inner oval area is about twice its width of 4 mm, the oval inductor is first considered as two adjacent circular 4 mm inductors having geometric contact at the center of the oval area and being electrically connected in series. Their currents are then opposed near the center and mainly cancel each other. This justifies the theoretical replacement. Now, the effective inner radius of the circular inductors is adjusted (2.3 mm) to make the sum of the two circular areas equal to the oval area (33 mm²). Due to the serial connection, the double of this (4.6 mm) is the radius to be used in Eq. (6) for the single effective circular inductor system. The procedure has proved itself in practice, e.g. in the case depicted by Fig. 18 below. The second transformer (Fig. 4(b)) was designed for a 35 W switched-mode LED power supply. It has embedded, cofired ferrite plates. Thus, it provides more area for surface-mounted devices (SMD) and achieves high integration density. The third design (Fig. 4(c)) combines an SMD-suitable surface with galvanic isolation in an e-car power inverter. Although a low power of 2 W suffices to drive the semiconductor switches on the secondary side, air cavities are embedded in addition to the ferrite core to avoid detrimental reverse impact of the fast-changing switched voltages through the parasitic coupling capacitance C_P.

The thickness of the ferrite plates is designed in such a way that their magnetic cross-section suffices to carry the magnetic flux, as given by Eq. (9), without exceeding half – or even better one third – of the saturation flux density of the specific ferrite material. Their best width is given by the diameter of the largest conductor turn plus the board thickness as excess width on both sides.

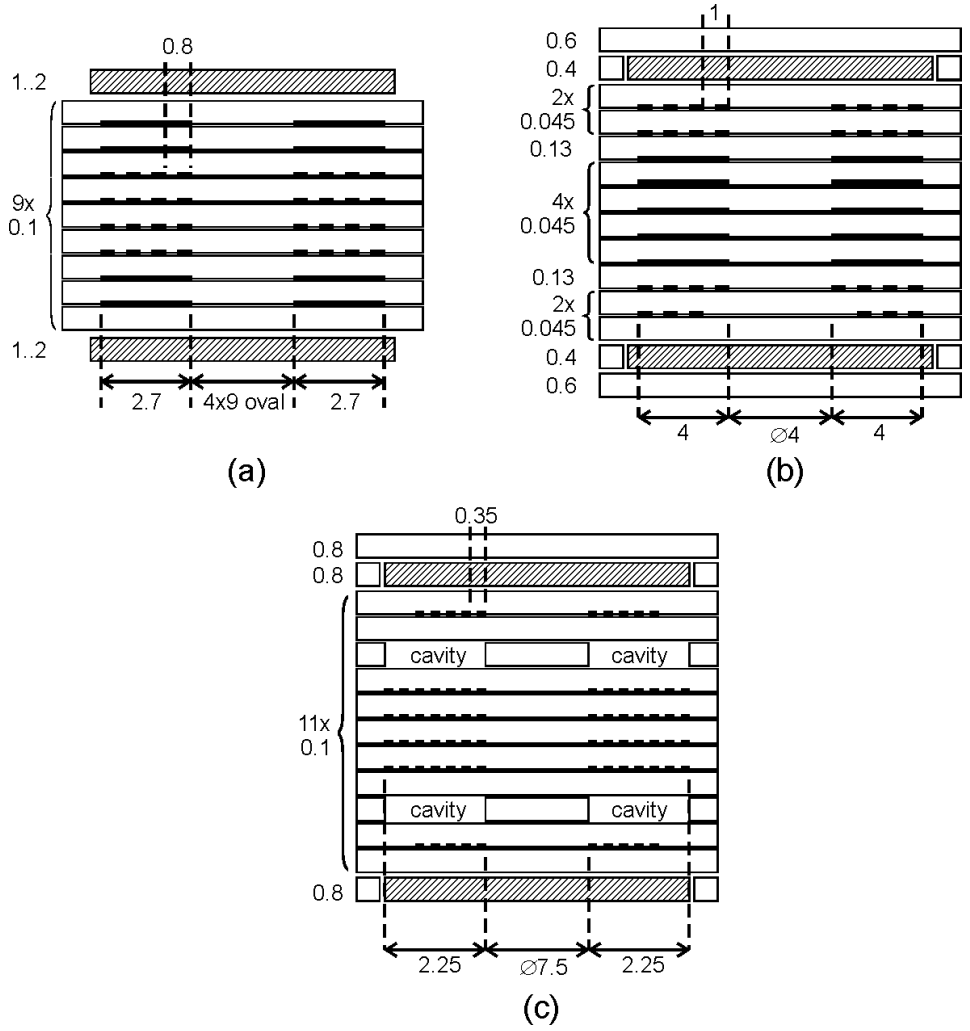

Fig. 4: Design examples for embedded transformers in dielectric LTCC boards: attached ferrite (a), embedded ferrite (b), and embedded ferrite with air cavities (c). The coil structures are: 16 inner primary turns (0.3 mm wide) with four outer secondary turns (2.7 mm wide) of oval shape, i.e. two half-circles of 2 mm radius with a straight section of 5 mm length in between (a), 15 outer primary turns (0.7 mm wide) with five inner secondary turns (4 mm wide) of circular shape (b), and ten outer primary turns with two inner secondary coils of 14 turns each, all conductors 0.15 mm wide.

IV. Embedding Technologies

Sintered ferrite cores can be directly embedded into cavities of a conventional printed circuit board (PCB) considering the design rules outlined above. Such widespread PCBs are multilayers made in a cost-efficient way by lamination of copper-clad organic layers without critical thermal processes. For high-temperature applications, however, ceramic multilayer boards made by means of LTCC technology are preferred. Now, advantageously, the dielectric and the magnetic tapes can be cofired at 900 °C. For a successful process, the ferrite must meet the following conditions:

(i) It develops useful magnetic properties when jointly sintered with the dielectric material.
(ii) Its sinter shrinkage and coefficient of thermal expansion (CTE) are properly matched to the dielectric to avoid cracks, delaminations, and warpage.
(iii) It is free from detrimental interaction with surrounding materials such as dielectric tapes and metal pastes.

Condition (i) has been addressed in our work by controlling sintering temperature, grain size, grain boundaries, and porosity based on ferrite composition, powder milling, and sintering additives. Achievement of condition (ii) by further adjustments to the ferrite was found difficult, if not impossible. Nevertheless, two successful approaches have been identified: The ferrite remains unmatched, but is mechanically decoupled from the dielectric by a sinter stop layer at the interface. In this case, both, the ferrite and the dielectric densify and sinter individually, but sinter bonding between the two materials is prevented at the interface. A sliding relative movement remains possible throughout the course of thermal processing. Cracks due to shrinkage differences are avoided. Alternatively, custom-made dielectric tapes offer degrees of control to match their sinter curve and CTE with those of the ferrite rather than vice versa. Failure-causing interface reactions according to condition (iii) were not encountered in our work, as a direct contact between particularly reactive metal traces and ferrite was avoided. As described in Sections IV (2) and IV (3) below and the references cited, Bi is used as an additive to lower the sintering temperature of the ferrites; Bi depletion therefore occurs near the ferrite-dielectric interface or at voids, which affects the local microstructure. However, when confined locally, these effects had no appreciable impact on permeability or inductance. Cofiring of a ferrite-dielectric combination that meets condition (i) but not (ii) will further be called nonmatched cofiring. When both conditions (i) and (ii) are met, it will be called matched cofiring.

(1) Measuring magnetic properties

Ferromagnetic LTCC tapes are commercially available but usually not compatible for cofiring with dielectric tapes in the volumes needed for power electronic applications. A specific development is required to achieve a better matching. While the sintering characteristics are analyzed by means of standard ceramic techniques on suitably shaped samples, the ferrites need a specific power electronic analysis of their relevant magnetic properties, to achieve quick convergence between demand and reality. To predict the performance of a specific ferrite as a transformer core in a circuit according to Fig. 3, its key magnetic quantities like amplitude permeability, magnetic loss, and magnetic saturation need to be measured on simple, easy-to-make test structures prior to investing excessive manpower. While planar capacitors with low stray fields are the device of choice for dielectric measurements, the equivalent device for magnetic properties is a simple ring core surrounded by several turns of copper wire. Such a toroidal coil of inner/outer diameters d_1/d_2 and height h is characterized by its magnetic cross-section $A_e \approx h(d_2-d_1)/2$, magnetic length $l_e \approx \pi(d_2+d_1)/2$, and the number of turns N. As the details of data analysis have been published before [28], only the essential relations will be given in the following. Ferrites exhibit nonlinear magnetic properties. Therefore, small-signal and large-signal data must be distinguished.

The complex small-signal permeability is derived from the impedance spectrum $Z(\omega)$ of the toroidal coil, taken with a commercial impedance analyzer (like HP4194A) in single-port configuration.

$$\mu'(\omega) - j\mu''(\omega) = \frac{2\pi}{\omega N^2 \mu_0 h \ln(r_2/r_1)} \left[Z''(\omega) - j\,(Z'(\omega) - R_0)\right], \tag{22}$$

where R_0 is the resistance of the copper wire and μ_0 is the vacuum permeability.

In the large-signal regime, permeability and loss depend in a nonlinear way on the exciting current. The data can be measured, for example, by applying a sinusoidal voltage through a signal generator and a power amplifier, e.g. the model SMY 01 by Rohde & Schwarz and the model 250L by Amplifier Research. The voltage transient $V(t)$ and the current transient $I(t)$ are stored on a digital oscilloscope, e.g. Tektronix TDS 520A. The instantaneous current and voltage signals during a full period yield the nonlinear relation between flux density B and magnetic field H, i.e. the hysteresis curve, through integration of the induction law

$$B(t) = \frac{1}{NA_e}\int_0^t U(t')\,dt' \quad \text{and} \quad H(t) = I(t)\,N/l_e \tag{23}$$

It was found satisfactory to derive further characteristics of the material from the fundamental waves with their amplitudes V_0, I_0, B_0, and H_0. The amplitude permeability μ and the total (resistive plus magnetic) volume-specific power loss P_L are then defined by

$$\mu = B_0/\mu_0 H_0 \tag{24}$$

$$P_L = \frac{\omega}{2\pi^2 h(r_2^2 - r_1^2)} \int_0^{2\pi/\omega} U(t) \cdot I(t)\,dt \tag{25}$$

(2) Mn-Zn ferrite

Mn-Zn ferrite can be tuned to specific applications based on its variable stoichiometry, designated by $(Mn,Zn)Fe_2O_4$. The exact composition is usually not known, since the focus is on the link between processing conditions and application performance. It is one of the most commonly used materials for power applications in the lower MHz regime. While its permeability tends to be higher than that of Ni-Cu-Zn ferrite, its lower gyromagnetic resonance frequency and hence a limited frequency

range of use must be taken into account. Other drawbacks like low specific resistivity, high permittivity, and sensitivity to excess oxygen during sintering have been overcome in the present context by device design and process control. While for conventional bulk material the calcination and the subsequent sintering are performed at 800 to 900 °C and 1 100 to 1 300 °C, respectively, commercially available ferrite powders are calcinated at about 1 200 °C in the present case to form a high-quality ferrite powder before sintering [32,33]. To support subsequent sintering at low temperature in nitrogen atmosphere, the powder is high-energy-milled and mixed with typically 2 % of Bi_2O_3-B_2O_3-SiO_2-ZnO glass (BBSZ) by volume as sintering aid [34]. Advantageously, the glass phase also raises the specific DC resistivity to more than 1 kΩ·m, while standard material typically exhibits only a few Ω·m [35]. The Curie temperature is 260 °C. The resonance frequencies (defined by $\tan\delta = \mu''/\mu' = 1$) of bulk and multilayer material are 6 and 15 MHz, respectively. Particularly relevant for power transformer design are amplitude permeability and power loss as given in Fig. 5.

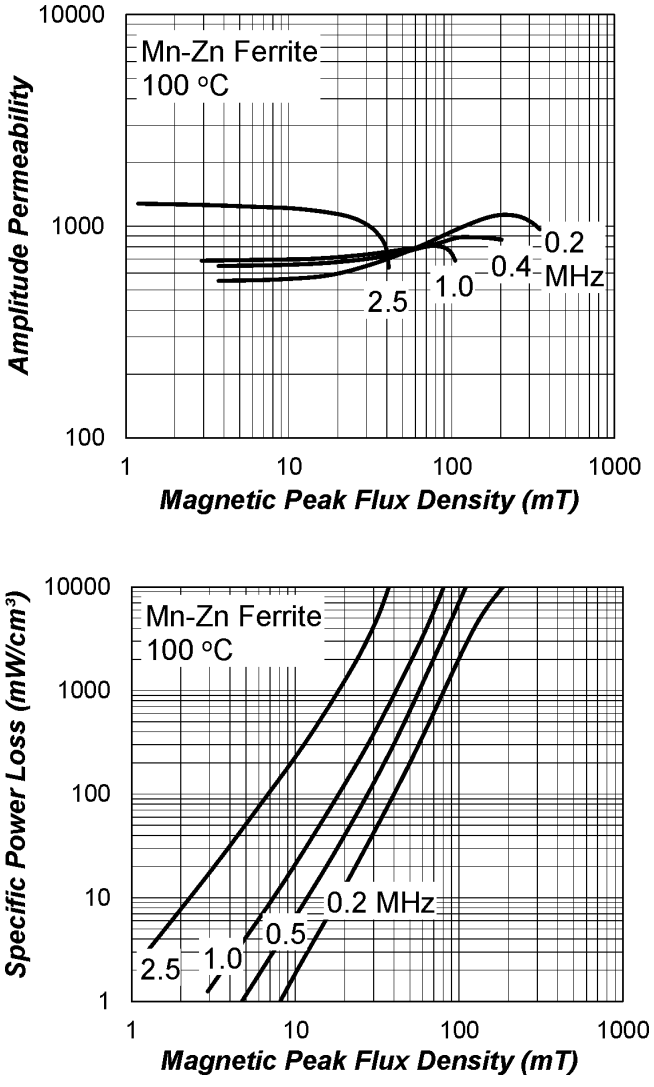

Fig. 5: Amplitude permeability and specific power loss of low temperature cofired Mn-Zn ferrite measured at 100 °C versus flux density at different frequencies.

Caused by resonant behavior, the amplitude permeability increases from 500 to 1 200 between 100 kHz and a few MHz, while the onset of saturation decreases from 400 mT to 40 mT. The cut-off in the amplitude permeability reveals magnetic saturation occurring at lower flux density for higher frequency. The volume-specific magnetic loss P_L of the ferrite can be approximated at 100 °C for an amplitude flux density of B_F between 1 mT and 100 mT and a frequency between 0.1 MHz and 3 MHz with the Steinmetz-type relation

$$P_L = \frac{5.6 \times 10^{-7}\,W}{m^3 T^{2.7} Hz^{2.7}} (B_F \cdot f)^{2.7} \tag{26}$$

Compared to commercial material [35] at 2.5 MHz and low flux, neither the total specific loss nor the amplitude permeability are appreciably deteriorated by the present modifications in composition and processing; however, magnetic saturation occurs at the lower flux density of 40 mT.

To obtain an expression for R_F, the circuit element for the magnetic loss, the whole flux according to Eqs. (9) or (10) is assumed to be coupled into the ferrite plates. If these have a combined magnetic length l_F and a magnetic cross-sectional area A_F, the flux density B_F is given by

$$B_F = \frac{\Phi}{A_F} \approx \frac{L_1 I_1}{N_1 A_F} = \frac{U_1}{\omega N_1 A_F}, \tag{27}$$

where the primary coil impedance is expressed as ωL_1. The total magnetic loss P_F, which is the product of the specific loss P_L and the volume of the two ferrite plates, is related to R_F by

$$P_F = l_F A_F P_L = \frac{U_1^2}{2R_F}. \tag{28}$$

The combination of these three equations yields

$$R_F = \frac{1.28 \times 10^8\,\Omega\,V^{0.7}}{m^{2.4}} \cdot \frac{N_1^{2.7} A_F^{1.7}}{U_1^{0.7} l_F}. \tag{29}$$

The coefficient contains units with fractional exponents due to noninteger Steinmetz parameters in Eq. (26).

(3) Ni-Cu-Zn ferrite

Ni-Cu-Zn ferrites are used for most multilayer ferrite inductors (MLFI) because of their easy sintering at low temperature in air and their good performance up to MHz frequencies [36,37]. A characteristic feature of low-firing ferrite compositions seems to be their need for a weak iron deficiency. Less than 50 mol% Fe_2O_3 is therefore used in the starting oxide mixture. Such iron-deficient compositions exhibit improved densification at 900 °C [38]. Then spinel compositions with less than two Fe atoms per formula unit are obtained, e.g. $Ni_{0.20}Cu_{0.20}Zn_{0.62}Fe_{1.98}O_{3.99}$. To enhance shrinkage and densification, sintering additives are frequently used. As an example, the addition of a mass fraction of less than 1 % Bi_2O_3 is effective to tailor microstructure formation and permeability [39,40]. Adversely, when Bi-doped Ni-Cu-Zn ferrite layers are integrated into LTCC modules, inhomogeneous Bi distribution and microstructure with loss of permeability occur [41]. It has been finally demonstrated, however, that additive-free Ni-Cu-Zn ferrite layers can develop a homogeneous, high-

ly permeable microstructure inside defect-free multilayer structures during cofiring with LTCC at 900 °C to 915 °C.

In this work, ferrite powders with compositions $Ni_{0.50-y}Cu_yZn_{0.52}Fe_{1.98}O_{3.99}$ ($0 \le y \le 0.25$) were prepared according to the mixed-oxide route. After mixing, calcination at 750 °C for 2 h, and subsequent milling in a planetary ball mill using zirconia as grinding medium, compacted samples were sintered at 900 °C in air. For the composition with $y = 0.20$, ferrite tapes were fabricated using a doctor-blade casting unit [42].

The shrinkage behavior of compacts of Ni-Cu-Zn ferrites with various Cu concentrations y was measured using dilatometry (Fig. 6). The Cu-free ferrite exhibits a broad shrinkage region around 1 050 °C, while shrinkage shifts to lower temperature with increasing Cu content. For $y = 0.20$, the shrinkage maximum appears at 870 °C. Samples with low Cu-content required a sintering temperature above 900 °C for densification, while those with $y \ge 0.20$ reached 97 % relative density or more at 900 °C.

The sintered ferrites exhibit homogeneous and fine-grained microstructures. As an example, the SEM micrograph of a $Ni_{0.30}Cu_{0.20}Zn_{0.52}Fe_{1.98}O_{3.99}$ sample with $y = 0.20$ is shown in Fig. 6; a mean grain size of about 2 µm is found. Closer inspection reveals that copper oxide precipitates at grain boundaries as a result of iron deficiency:

$$Ni_{1-x-y}Cu_yZn_{x+z}Fe_{2-z}O_{4-z/2} \rightarrow \left(\frac{2-z}{2}\right) Ni_{\frac{2-2x-2y}{2-z}}Cu_{\frac{2y-3z}{2-z}}Zn_{\frac{2x-2z}{2-z}}Fe_2O_4 + \frac{3z}{2}CuO \qquad (30)$$

Nominally Fe-deficient compositions transform into a stoichiometric spinel somewhat poor in Cu and CuO, which segregates at the grain boundaries and thus favors densification at 900 °C. Stoichiometric compositions with $z = 0$ require a higher sintering temperature, because this segregation mechanism of Cu is absent [38].

As the material $Ni_{0.30}Cu_{0.20}Zn_{0.52}Fe_{1.98}O_{3.99}$ ($y = 0.20$) turned out to exhibit excellent sintering and densification behavior at 900 °C [42], it was the focus of the subsequent studies. Fig. 7 shows the permeability vs. frequency and the specific power loss vs. flux density for a ferrite multilayer laminate sample, sintered at 900 °C for 2 hours in air. The real part µ′ of the permeability is 340 at 1 MHz, while the imaginary part µ″ peaks near 20 MHz. Moreover, it was demonstrated that this ferrite can be sintered at 900 °C in air and in reduced oxygen partial pressure down to 1 kPa as well [43]. Below 0.1 kPa, cuprous oxide is formed and the permeability is reduced.

In summary, the Ni-Cu-Zn ferrite with $y = 0.20$ has shrinkage characteristics that enable low-temperature sintering at 900 °C. Without sintering additives, a homogeneous ceramic microstructure is obtained exhibiting a relative permeability of 340 and a Curie temperature of 220 °C.

(4) Adapted dielectric

Shrinkage of commercial dielectric LTCC tapes such as DP 951 (DuPont, Research Triangle Park, NC, United States) or CT 707 (Heraeus, Hanau, Germany) is completed during the heating-up period at temperatures clearly below 900 °C. By contrast, both of our ferrites are not fully densified during heating-up period. Complete densification of ferrite tapes needs a long dwell time at a temperature of at least 900 °C. Furthermore, ferrites have significantly higher coefficients of thermal expansion (CTE) in comparison to standard dielectric LTCC materials. Therefore, tailored dielectric tapes need a CTE in the range of 10 ppm/K and shrinkage at higher temperature. Appropriate dielectric materials coded as BAM562 and BAM474 were developed for cofiring with the Mn-Zn and Ni-Cu-Zn ferrites described in sections IV (2) and IV (3), respectively.

Starting compositions of both glass ceramic composites comprise glass and two crystalline components, alumina and quartz. Quartz exhibits a high CTE of about 15 ppm/K and was thus used as dispersed phase to increase the thermal expansion of the composite material. Based on Priven's model [44], glass compositions with adapted glass transition temperature and viscosity were calculated. The development and characterization of the dielectric materials have been reported before in detail for BAM562 [45] and for BAM474 [41, 42, 46].

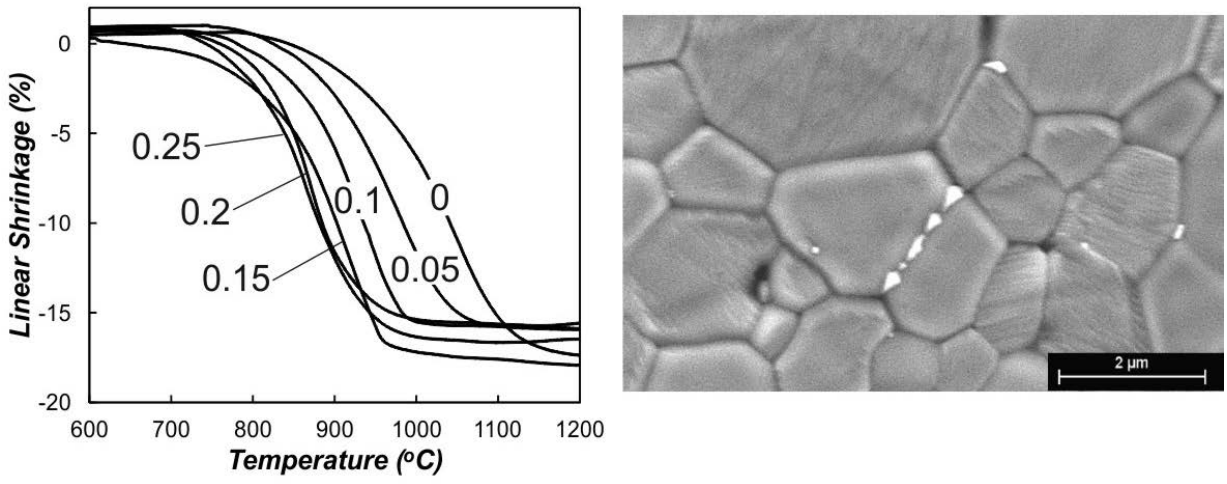

Fig. 6: Shrinkage of green compacts of $Ni_{0.50-y}Cu_yZn_{0.52}Fe_{1.98}O_{3.99}$ versus temperature with the variable Cu content y as parameter (left), and SEM micrograph of a typical microstructure of a sample with y = 0.20, sintered for 2 hours at 900 °C in air (right).

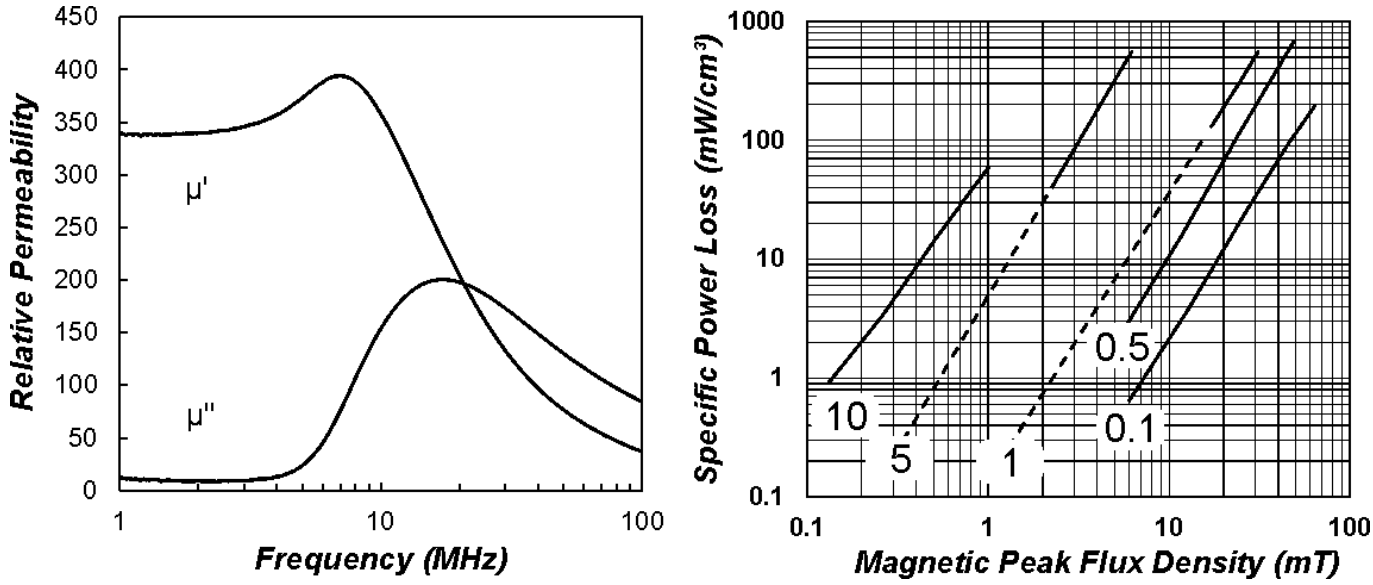

Fig. 7: Permeability vs. frequency (left), and power loss versus flux density at different frequencies indicated in MHz (right) for $Ni_{0.30}Cu_{0.20}Zn_{0.52}Fe_{1.98}O_{3.99}$.

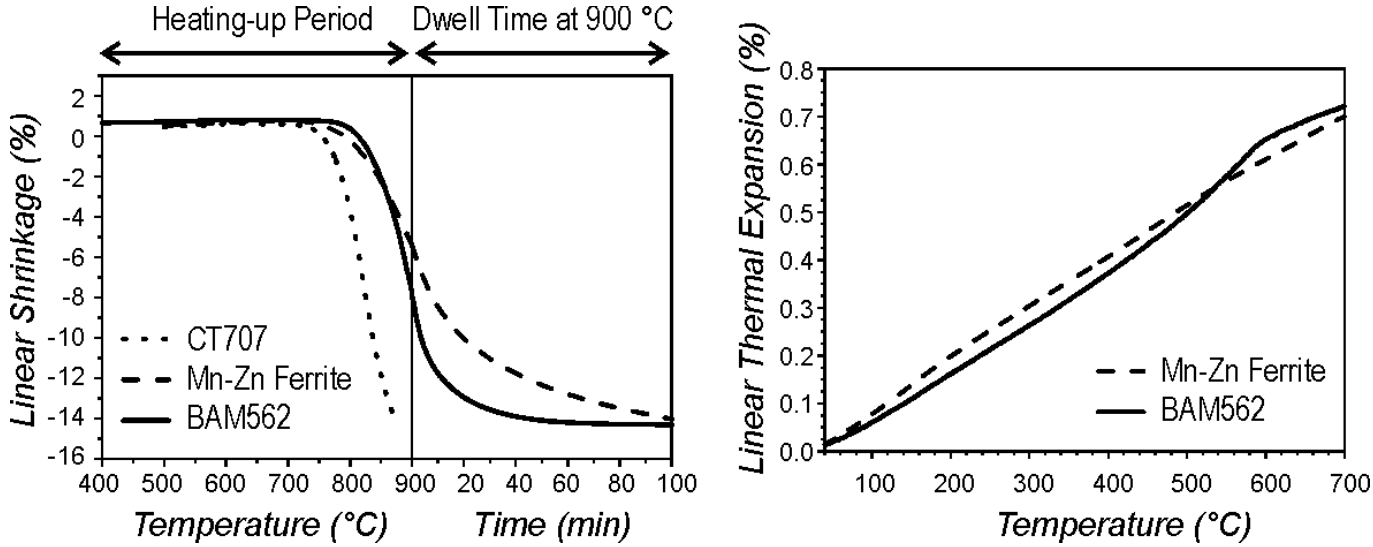

Fig. 8: Shrinkage curves during heating-up period and dwell time at 900 °C (left) and linear thermal expansion between room temperature and 700 °C (right) of Mn-Zn ferrite and BAM562 dielectric material.

Shrinkage curves of Mn-Zn ferrite, BAM562, and commercial CT707 tapes during heating-up with 5 K/min to 900 °C and subsequent dwell time are depicted in Fig. 8 (left). Compared to standard dielectric tapes, adapted BAM562 dielectric tape shows a shifting of the shrinkage curve to higher temperatures because of increased glass viscosity. As a result, onset of shrinkage and shrinking behaviour of BAM562 during the heating-up period is well adapted to that of Mn-Zn ferrite. Both tapes are characterized by a high amount of shrinkage during dwell time at 900 °C. However, a difference in shrinkage progression remains between Mn-Zn ferrite tape and the dielectric tape. The dielectric densifies faster than the ferrite. The very slow densification of the ferrite could not be fully replicated. Thermal expansion curves of dense Mn-Zn ferrite and BAM562 dielectric material below the glass transition temperature are shown in Fig. 8 (right). Almost identical linear length contraction of 0.70 % for Mn-Zn ferrite and 0.72 % for BAM562 in the temperature range between 700 °C and room temperature prove an excellent adaptation of thermal expansion behavior. The nonlinearity of BAM562 around 600 °C is caused by a reversible phase transition of quartz, so-called quartz inversion.

Shrinkage behavior of additive-free Ni-Cu-Zn ferrite is shown in Fig. 9 (left). Characteristics are shrinkage onset at about 660 °C, 14 % linear shrinkage during heating-up period and total shrinkage of about 18 % after 1 h dwell time at 900 °C. Shrinkage curves of ferrite and BAM474 dielectric progress almost identical throughout the process. Small differences are visible in the early sintering stage: The BAM474 dielectric exhibits a delayed onset of shrinkage; however, a steeper progression compensates for the lag up to approximately 860 °C. As shown in Fig. 9 (right), the CTE curves of ferrite and dielectric are well adapted. Identical linear length contraction between 700 °C and room temperature of 0.64 % were measured for Ni-Cu-Zn ferrite and BAM474.

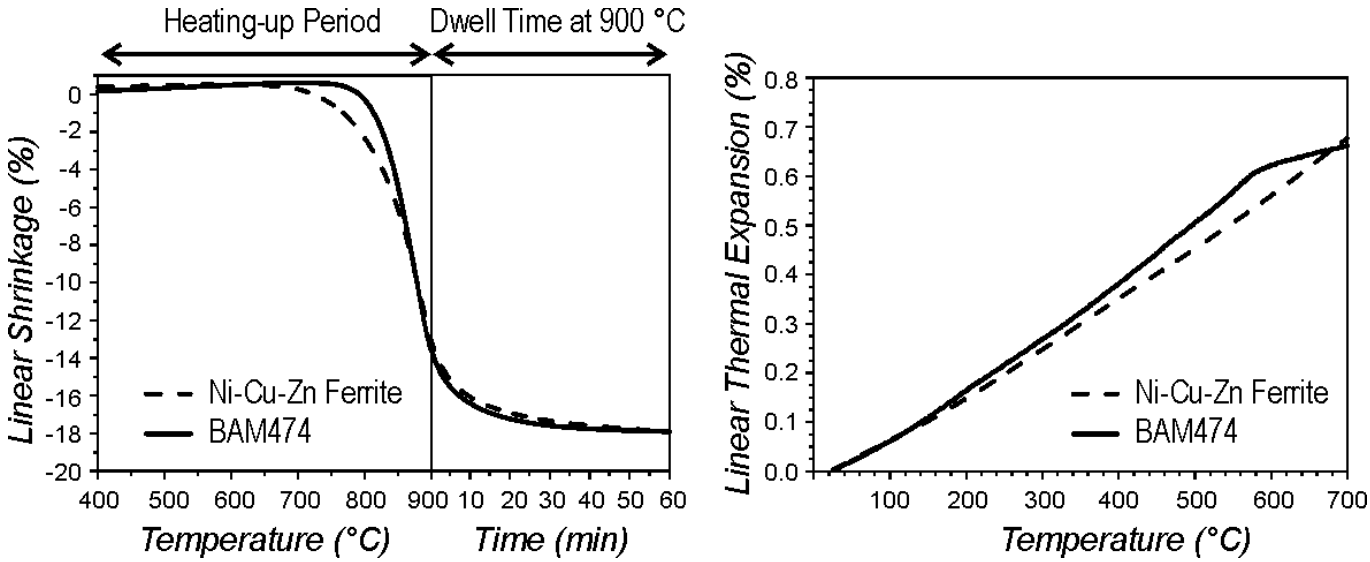

Fig. 9: Shrinkage curves during heating-up period and dwell time at 900 °C (left) and linear thermal expansion between room temperature and 700 °C (right) of Ni-Cu-Zn ferrite and BAM474 dielectric material.

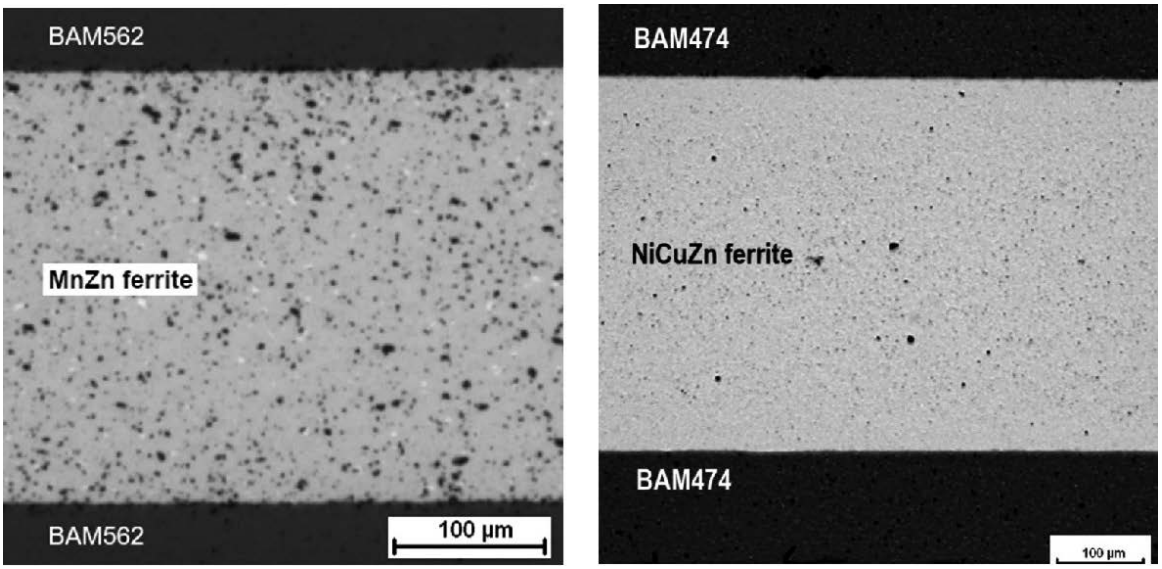

Fig. 10: Cross-sections of cofired multilayer samples, Mn-Zn ferrite between BAM562 tapes (left) and Ni-Cu-Zn-ferrite between BAM474 tapes (right).

(5) Matched cofiring

Symmetrical stacks, consisting of Mn-Zn ferrite tapes and BAM562 dielectric tapes or Ni-Cu-Zn ferrite tapes and BAM474 dielectric tapes, were set up and isostatically laminated at 75 °C and 25 MPa for 10 minutes. Mn-Zn/562 and Ni-Cu-Zn/474 laminates were debindered in air at 500 °C with a heating rate of 0.5 K/min and a dwell time of 1 hour. Mn-Zn/562 laminates were heated up with 5 K/min to 900 °C and sintered for 8 hours in nitrogen atmosphere with an oxygen partial pressure p_{O2} of approximately 10^{-5} bar. Differing from this, sintering of Ni-Cu-Zn/474 laminates was performed in air at 915 °C for 2 h.

Both multilayer types exhibit a flat surface after cofiring, delamination or cracking are not observed (Fig. 10). All cofired materials exhibit sintered densities similar to separately sintered materials. No open porosity was detected. Analyzed material properties and the microstructures shown in Fig. 10 confirm an adequate adaptation of sintering curve and CTE of the respective multilayer components.

There are partly contradictory demands on interfaces between ferrite and dielectric tapes. Strong bonding is necessary. At the same time, an extended reaction zone and the formation of new phases should be avoided. Furthermore, minimized diffusion is requested to prevent degradation of permeability. Comprehensive investigations of element diffusion between ferrite and dielectric layers were carried out by means of electron microprobe analyses, both in Mn-Zn/562 multilayers [45] and Ni-Cu-Zn/474 multilayers [41]. The interface zones meet the aforementioned demands in both multilayer types. Interface regions of about 20 µm thickness were found in both material combinations as a result of elemental diffusion from the ferrite into the glassy phase of the dielectric. Significant diffusion in the opposite direction was not detected.

Despite promising interfaces and microstructure, Mn-Zn ferrite reaches a relative permeability of only 100 be-

tween the dielectric tapes, much less than the value of 500 without dielectric embedding. Separately sintered Mn-Zn ferrite consists of stoichiometric (Mn, Zn)Fe_2O_4 spinel and traces of hematite (Fe_2O_3). By contrast, remarkable amounts of Fe_2O_3 were found in the cofired ferrite, indicating a degradation of the spinel due to substitution of Fe^{3+} by Mn^{3+} ions. It is supposed that the dielectric enclosure impedes the gas exchange during sintering. Thus, the oxygen partial pressure inside the ferrite and the oxidation state of manganese ions are out of balance. The mechanisms of phase formation and permeability evolution were resolved in detail by means of light microscopy, SEM, EDX, and XRD investigations joined with thermodynamic calculations [45].

Unlike Mn-Zn ferrite, the magnetic permeability of (Bi_2O_3-free) Ni-Cu-Zn ferrite was not significantly affected by cofiring. Permeabilities of 480 and 470 were measured without and with dielectric cladding, respectively [42].

The transformer design according to Fig. 4(b) calls for the arrangement of ferrite layers and silver conductors between dielectric tapes. Owing to the reduced permeability of Mn-Zn ferrite between dielectric tapes, only Ni-Cu-Zn/474 laminates were further investigated with integrated conductors.

Diffusion of silver from inner conductors and vias is a well-known critical high-temperature process in the production of LTCC modules. Mechanisms of silver transport from the conductor pattern into LTCC glassy phase were intensively investigated in previous work [43, 47]. Silver diffuses in the glassy phase of surrounding materials, causes a reduction of the glass viscosity and, consequently, changes the sintering behavior around silver lines. This becomes relevant at process temperatures above 750 °C and it increases with rising temperature, provided that open porosity in ambient dielectric material allows for transport of oxygen to the silver conductor interface. Open porosity disappears at temperatures around 800 °C in most standard dielectric materials. Hence, in such materials silver oxide formation is interrupted early and silver diffusion can be neglected. Unfortunately, for compatibility with Ni-Cu-Zn ferrite, BAM474 was designed for higher sintering temperature. This longer silver diffusion in Ni-Cu-Zn/474 laminates now gives rise to inhomogeneous shrinkage and pronounced warpage [43].

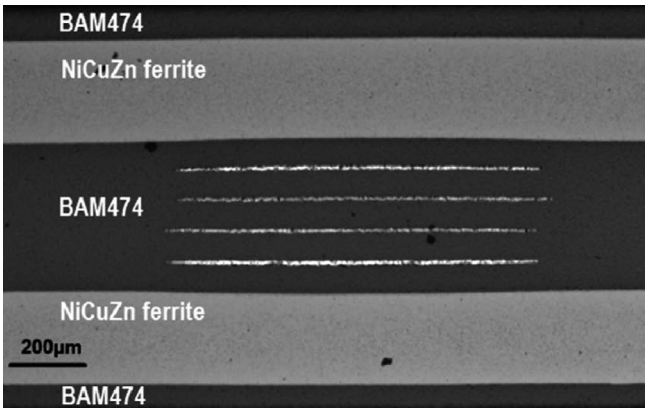

Fig. 11: Ni-Cu-Zn/474 multilayer with silver conductors, cofired in nitrogen atmosphere.

Of course, the oxidation of silver and its diffusion into the glassy phase may be prevented by sintering in nitrogen atmosphere [47]. The nitrogen-sintered thin Ni-Cu-Zn/474 laminate in Fig. 11 exhibits in fact intact dielectric, ferrite, and conductor layers. Unfortunately, Ni-Cu-Zn ferrite segregates cuprite (Cu_2O) and loses permeability under these conditions, see Table 1.

Table 1: Permeability of Ni-Cu-Zn ferrite in dependence on oxygen/nitrogen ratio of sintering atmosphere.

	Sintering atmosphere at 100 kPa total pressure			
Oxygen content (%)	21	1	0.1	0.001
Permeability at 2 MHz	474	480	230	220

As suggested by Table 1 and confirmed by a combined XRD/thermogravimetric study [43], the Ni-Cu-Zn ferrite is stable at an oxygen partial pressure of 1 kPa or higher. Thicker materials like the transformer of Fig. 4(b) nevertheless exhibited defects after sintering at 1 kPa oxygen partial pressure. Silver diffusion and its consequences are obviously not sufficiently suppressed under these conditions. Further lowering the oxygen partial pressure, however, is effective, as the ultrasonic and light microscopic analysis on a transformer sintered at 0.2 kPa oxygen partial pressure reveals (see Fig. 12). Neither delaminations (left) nor silver diffusion (right) are detectable. The

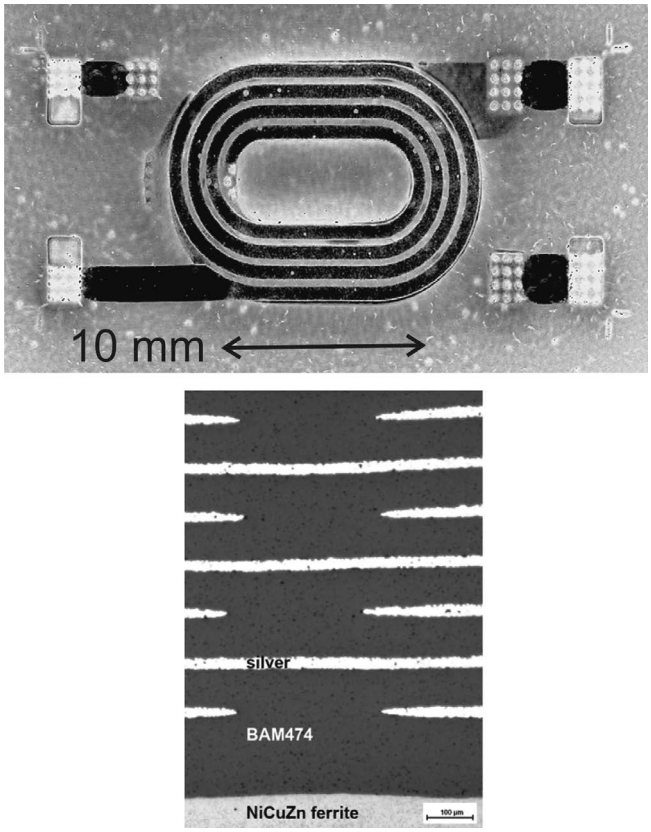

Fig. 12: Transformer sintered at 915 °C/2 h, heating rate 4 K/min and $pO_2 = 0.2$ kPa. Ultrasonic scan (front view, left) and dielectric layers with embedded silver conductors (cross-section, right).

matched cofiring of intact transformers is thus demonstrated. However, this approach trades the "matching" of the materials against a restricted choice of dielectric tapes and an obviously unavoidable degradation of permeability. In view of Eq. (4) and the associated previous discussion further examinations would be needed to decide, if a limited degradation is tolerable on device level.

(6) Nonmatched cofiring

Despite the lack of matching between the low-temperature Mn-Zn ferrite described before and the commercial dielectric LTCC tapes, a useful, simple, and reliable cofiring process has been conceived. At first, Fig. 13 indicates a severe mismatch in sinter shrinkage of both materials. While the onset of sintering is at 600 °C for the dielectric, the threshold is at 800 °C for the ferrite. When the ferrite is placed in a closed cavity inside the dielectric, the cavity must be designed larger to account for 25 % shrinkage of the dielectric with no shrinkage of the ferrite below 800 °C.

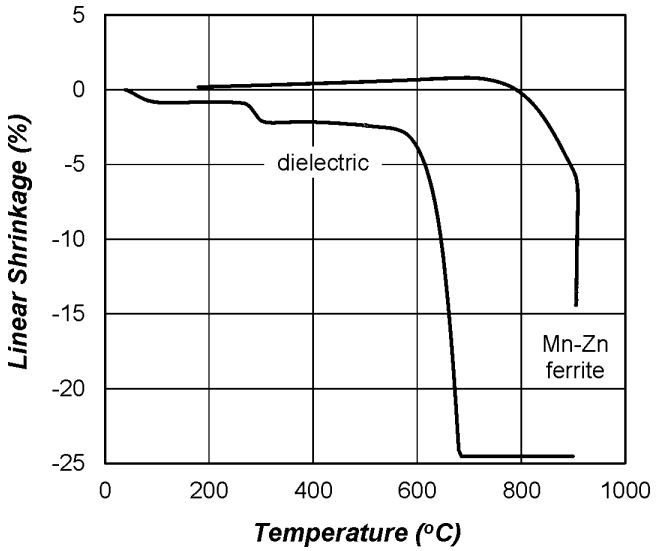

Fig. 13: Measured shrinkage mismatch between Mn Zn ferrite (as described in Section IV (2)) and commercial dielectric LTCC material (DuPont 951) at 5 K/min heating rate.

Advantageously, the coefficient of thermal expansion of the ferrite is 10 ppm/K (Fig. 8), almost twice that of the dielectric of 6 ppm/K. Therefore, the ferrite contracts stronger with decreasing temperature after sintering. During both processes, heating and cooling, however, it is essential that ferrite and dielectric can move freely in respect of each other and that a sintered fusion is suppressed. Alumina-filled paper was found to be effective as such sinter stop at the interface [48]. The paper was inserted during the lamination process. It contained mass fractions of 60 % alumina powder, 20 % pulp and 20 % carbon fiber. While pulp and carbon burn out at 350 °C, the alumina powder stays in place as an inert loose interface layer.

Board-integrated transformers with embedded Mn-Zn ferrite, designed after Fig. 4(b), exhibit a flat surface (Fig. 14). However, the cross-sectional image seems to indicate a slight convex bend owing to a vertically narrow cavity. This has obviously also caused short, inoffensive delaminations at the cavity edges. The ferrite plates appear to be retained as desired by alumina particles below and above (not resolved by the image).

(7) High-current-rating conductors

Conductors embedded inside power-electric circuit boards must be able to transport currents of several Amperes at justifiable resistive loss. The present transformer designs have been examined from this point of view to identify a potential need for modification in design or manufacturing. While resistive conductor loss is of lower concern in traditional printed circuit boards with their bulk copper conductors, LTCC relies on screen printing of pastes containing metallic particles (Ag, AgPd, AgPt or Au). Layer thickness and specific conductivity are therefore lower. Furthermore, ceramic green tapes exhibit lower plasticity than organic board materials, thus impeding the adaptation of thick conductor traces.

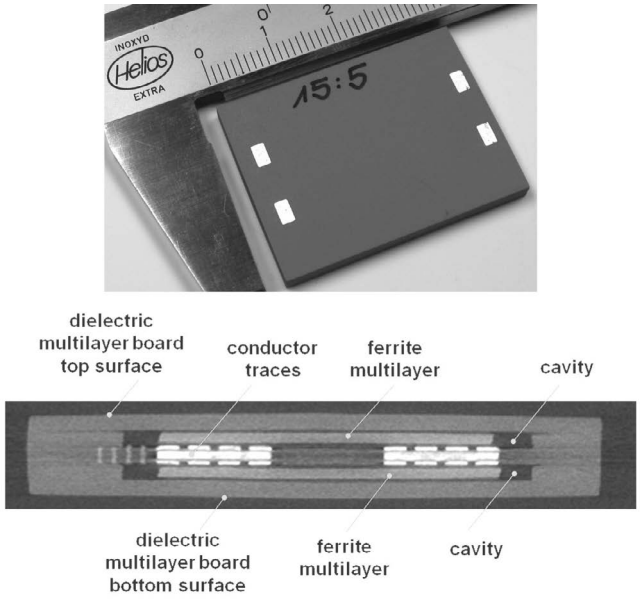

Fig. 14: Photograph and cross-sectional computed tomography (CT) image through the center of an embedded transformer made according to the design of Fig. 4(b). Silver conductors appear in white. Owing to the limited CT resolution, however, the five broad central secondary turns and the adjacent two conductor layers with narrower primary turns below and above are blurred. As indicated by Fig. 4(b) the outer diameter of the turns is 12 mm.

To test the adequacy of standard screen printing, the resistances of the primary and the secondary coils R_1 and R_2 are calculated under DC conditions from their layout in Fig. 4, their thickness of typically 10 µm and the specific resistivity of the silver paste after firing (1.8×10^{-8} Ω·m). Assuming an ideal transformer, this yields an effective loss resistor $R_{\text{eff}} = R_2 + (N_2/N_1)^2 \cdot R_1$ on the secondary side. In relation to the secondary load, R_{eff} provides a coarse estimate for the power fraction lost in the conductors, see Table 2.

Despite its high load resistance, it is particularly design (c), which suffers from narrow traces, numerous turns, and a higher fraction of resistive loss. Even worse, all these transformers are not ideal and less power actually reaches the load. Real transformer performance is obtained only from Eqs. (20) and (21) using at least estimated values for

the parasitic elements. The final confirmation additionally requires a measurement-based revelation of the equivalent circuit as described below in Section V. Such elaborate data is shown for the present designs in Fig. 15. Although the estimates in Table 2 are essentially confirmed near the operating frequencies around 2 MHz, the transformers (b) and (c) exhibit slightly or even considerably higher losses of 5 % and 10 to 15 %, respectively. It appears therefore advisable to consider a redesign in case (c) aiming at a conductor thickness of 30 to 50 µm. However, without compensating measures, the conventional screen printing and lamination process would cause an inhomogeneity of the ceramic green density with subsequent warpage of the multilayer and cracking or chipping during sintering. To provide the space needed for the additional conducting material, the technical solutions published so far, combine embossed or laser-ablated trenches in the green tape with printed silver paste or metallic silver inlays.

Initially, the embossing of trenches in commercial tapes prior to conductor deposition was studied [49, 50]. Mould depths of up to 30 % of the green tape thickness were found feasible, e.g. for DuPont 951 tapes. Conductors were defined photolithographically from a screen-printed, ultraviolet-sensitive thick film ink (DuPont 6453), which is stabilized in UV-exposed areas and spray dissolved in unexposed areas. The resulting conductor thickness was 40 µm, four times the standard value.

Table 2: Estimation of power fraction lost as heat in transformer coils.

Transformer design	(a)	(b)	(c)
Ratio of turns N_2/N_1	4/16	5/15	28/10
Primary coil R_1 (Ω)	2	1	1
Secondary coil R_2 (Ω)	0.05	0.05	10
Secondary load R_L (Ω)	50	4	540
Effective loss R_{eff} (Ω)	0.175	0.16	33.5
Relative resistive loss (%)	0.4	4	6

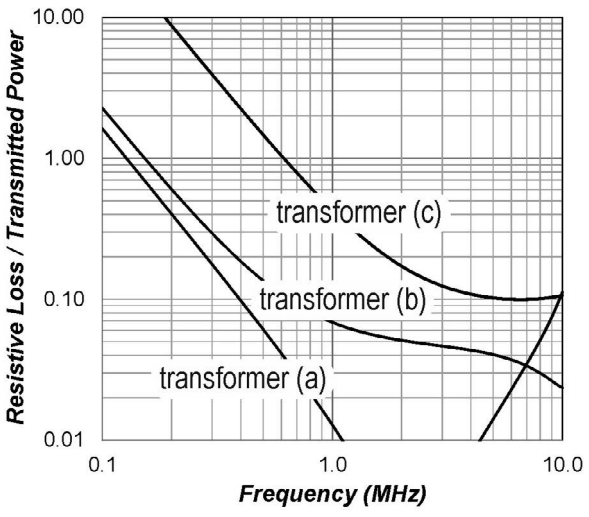

Fig. 15: Calculated resistive loss in transformer coils in relation to the power transmitted to the load.

In an alternative approach, the limitations of plastic deformation and perturbance of the green tape are overcome by ablating the trench material with a laser. This is a serial process, but in a carefully selected processing window uneven and rough trench bottoms or glassy residuals can be avoided [51]. The deeper trenches can even incorporate silver foils of more than 100 µm thickness for improved thermal management [52]. For complex conductor geometries, however, this inlay solution is inefficient.

We therefore pursued a combination of laser-ablated trenches with stencil-printed conductors for the present work. Conventional screen printing of conductors is known to be insufficient, since the metallic paste does not reach the deep trench bottom through the screen mesh [52]. As multiply connected coil structures cannot be fabricated with simple stencil apertures, a specific design with 800-µm-wide supporting ligaments in a 50-µm-thick stencil was used as shown in Fig. 16. To optimize filling, drying, and shrinking of the thick silver paste, its rheological behavior was adjusted with reduction of the solid phase content. Also, application of unidirectional pressure during sintering was required to secure connectivity at all materials interfaces. Up to 120 µm-deep trenches were filled and superfluous metal paste was removed by laser cleaning prior to lamination of the layers [53]. The potential of the technique is evidenced by the conductor cross-sections in Fig. 17 characterized by 80-µm-high conductors with line and space widths of 70 µm and 30 µm, respectively. Local voids and delaminations are recognizable but proved insignificant in reliability tests; after eight weeks of thermal cycling between - 40 °C and 220 °C the defect rate was below 2 %.

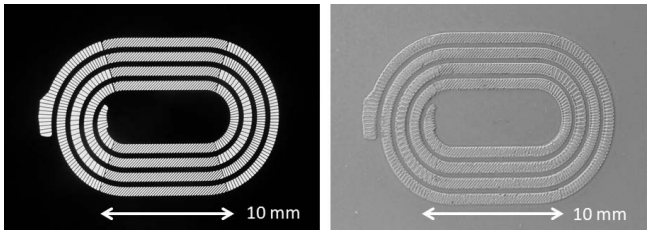

Fig. 16: The 50-µm-thick metal stencil for a planar coil with 800-µm-wide ligament-like stabilizing structures in curved sections (left) and print result (right).

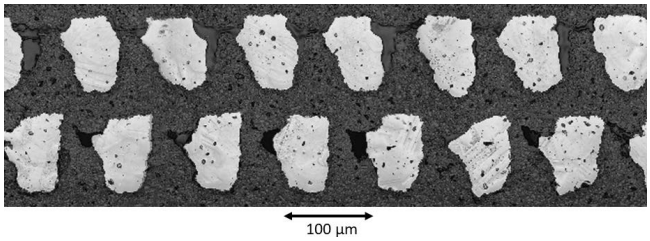

Fig. 17: Cross-sectional view of conductors with high aspect ratio.

The decision about application of enhanced conductor technology requires a balanced consideration of the processing complexity added against the advantages gained on the component level. To this end, we refer to Fig. 20

below, which depicts the performance analysis of transformer (c) in its embodiment of Fig. 4. Thicker conductors would necessitate raising the ceramic layer thickness from 100 µm, as realized, to at least 130 µm. A simulation based on Eqs. (10), (11) for this increased air gap between the two embedded ferrite plates reveals 20 % lower inductances but only marginally lower magnetic coupling. Proceeding to Eq. (21), it was found, that a correspondingly reduced stray inductance would improve low frequency performance in the 100 kHz range. At the operating frequency of 2.5 MHz the same power of 1.1 W would be transmitted, however, with an efficiency increase from 74 % to 80 %. Finally, this effect of saving 60 mW of power on the primary side appeared too marginal to replace screen printing with laser ablation and stencil printing.

V. Functional Verification

(1) Device level

The inductive and capacitive circuit elements of the transformers were all determined by calculating the insertion loss S_{21} using Eq. (18) and fitting it to the measured insertion loss [32]. As the match between model and measurement is sufficiently accurate between 0.1 and 30 MHz, the procedure reveals the "measured" circuit elements. The magnetic coupling unambiguously results from the constant level at medium frequencies, typically between 1 and 10 MHz. Below this range, the primary inductive impedance is low and more or less shorts power input; at high frequencies, power transmission to the load is usually impeded by the parallel capacitance C_P. Additionally, the serial capacitance C_S can be derived from the band-stop frequency that shows up owing to its interaction with the leakage inductances. Table 3 compiles these circuit elements for the three designs of Fig. 4.

Table 3: Equivalent circuit elements obtained for Mn-Zn ferrite transformers from measured insertion loss spectra.

Transformer design	(a)	(b)	(c)
Ratio of turns N_2/N_1	4/16	5/15	14/10
Primary main inductance L_1 (µH)	53	6.9	4.6
Secondary main inductance L_2 (µH)	3.3	0.8	9.1
Coupling coefficient k	0.96	0.94	0.86
Parallel capacitance C_p (pF)	300	300	10
Serial capacitance C_s (pF)	150	250	8

Despite similar turn numbers of designs (a) and (b), the size of (a) yields much larger inductance. Furthermore, the thick attached ferrite seems to catch field lines more efficiently than the thin embedded one, leading to better coupling. Transformer (c) has the same lateral extension as transformer (b) but almost twice the dielectric thickness, i.e. air gap between the ferrite plates, which drives magnetic coupling down to 86 %. On the other hand, the narrow conductor traces and the integrated air gaps yield a considerable reduction of capacitive coupling in this case.

To compare the measured values of Table 3 with predictions of Eqs. (6) to (12), Fig. 18 shows the main inductances as circle positions and the leakage as circle diameter. Generally, the measured (thick line) and predicted (thin line) data are in practical agreement, i.e. the model works. This is particularly true for the conversion of the oval transformer (a) into an effective circular one as described before in Section III (3). However, it seems to overestimate the inductances, when the ferrite is embedded. Obviously, such thin ferrite plates do not completely capture the magnetic field lines, so that the real devices lag behind the perfect model. Although driven to the limits of miniaturization as intended, the devices are nevertheless fully functional. Having passed approval under small-signal conditions the model is now to be carried on to power analysis in target applications by applying Eqs. (19) to (21).

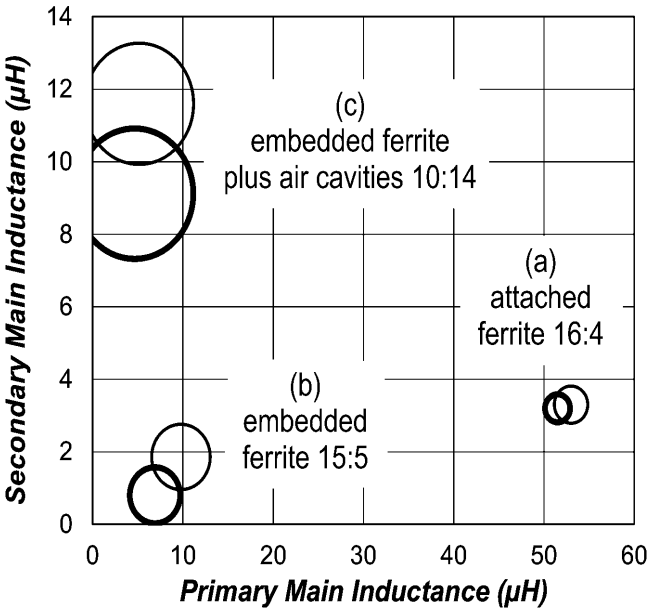

Fig. 18: Main inductance map showing L_2 vs. L_1 for the three transformer designs as indicated. Circle diameters indicate the leakage 1-k, ranging from 3 % to 14 %. Heavy lines denote measured data of Table 3, thin lines show data calculated according to the theory in Section III.

(2) Application level

The transformer type (b) was designed and is used for galvanic isolation in a switched-mode power supply (SMPS) integrated inside a 1000 lm/30 W LED lamp socket. To achieve a compact, integrable transformer size, the SMPS converts the rectified line voltage by MOSFET switches to a 2 MHz input power on the primary side. The whole power passes the transformer. On the secondary side, a rectifier and the LED array form an essentially resistive load of 5 Ω, which is visible as 45 Ω on the primary side due to the ratio of turns.

The power and efficiency spectra shown in Fig. 19 were calculated from Eq. (21). Measured results at 2 MHz, as indicated by circles, confirm the validity of the design approach. The design target, to achieve a constant level of output power over a relevant frequency range near the the-

oretical value of $50\ V^2/2{\cdot}45\ \Omega = 28$ W with high efficiency, has been met. To optimize turn numbers, magnetic coupling and parasitic elements, it was of considerable benefit that modifications could be applied easily and their effect could be calculated fast. The rise of input power at low frequency and the decrease of both, input and output power, at higher frequency are characteristic and are attributed to low inductive impedance and blocked transmission by the C_S-induced bandstop, respectively. To further assess the quality of this result, a conventional, three-dimensional transformer with the same number and size of turns was made from free-standing enameled copper wire (0.5 mm thick). An E-shaped commercial core [35] of 4.8 mm diameter ensured maximal magnetic coupling in this case. The triangular symbols in Fig. 19 indicate that the 3D type has better measured power efficiency than the 2D version as a consequence of lower conductor and ferrite losses. However, the performance impairment of the embedded transformer appeared manageable, making it far more attractive owing to its enormous size benefit of 290 mm^3.

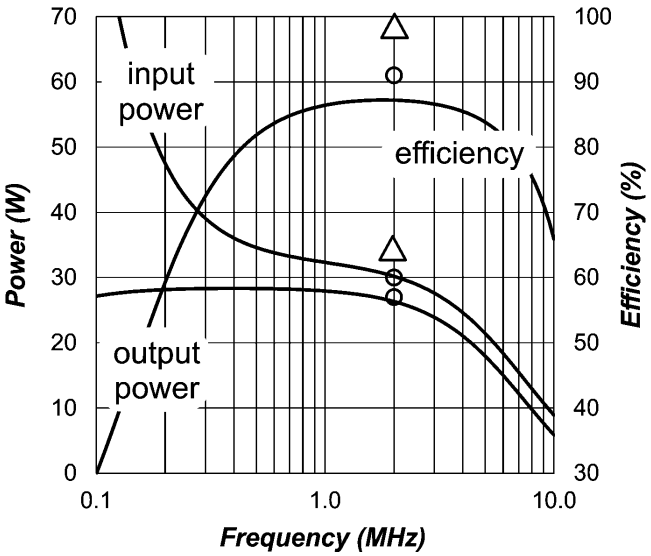

Fig. 19: Input power, output power and efficiency of transformer (b) vs. frequency for a primary voltage amplitude of 50 V and a secondary load of 5 Ω. Lines are predicted with the present model. Symbols at 2 MHz indicate measured data of the embedded LTCC transformer (circles) and of a conventional wire-wound reference transformer with E-shaped ferrite core (triangles).

As a second example, we consider, how power inverters for electric vehicles benefit from embedded, thermally robust transformers. Such devices change direct current from the battery to alternating current for the electric motor. In our device, two insulated gate bipolar transistors (IGBTs) connected in series shape the required waveform by means of pulse width modulation of the battery voltage of 400 V. An application-specific integrated circuit (ASIC) controls the switching of the transistors by applying appropriate control signals through driver circuits to their gates. As both, the IGBTs and their gate drivers, are subject to heavy voltage changes in the power stage, data and power are transmitted to the drivers through a capacitor and a transformer of present design (c), respectively. Being interposed between the sensitive ASICs and each of the two gate drivers, these components provide galvanic isolation and over-current protection.

To supply power to the gate driver an internal capacitor C is charged by the rectified output voltages of the center-tapped transformer. The equivalent circuit is given by the inset in Fig. 20. If the diodes have low resistance, harmonic analysis and charge conservation reveal that the capacitor is charged to a voltage equal to the DC component of the fully rectified sine wave, i.e. $2V_s/\pi$, where V_s is the sine wave amplitude delivered by a single secondary transformer coil. The driver's current and power consumption are therefore $2V_s/\pi R$ and $4V_s^2/\pi^2 R$, respectively. As the diodes mutually decouple the two secondary coils, each coil contributes individually one half of the total power, i.e. $P = 2V_s^2/\pi^2 R$. Hence, the visible impedance per coil is $R_{vis} = V_s^2/2P = \pi^2 R/4 = 271\Omega$. By calculating V_s for this load, the power transmission $4V_s^2/\pi^2 R$ to the driver circuit results as shown in Fig. 20. In agreement with measurements, the transformer is able to supply a power of 1 W with 74 % efficiency to the gate driver from 15 V input amplitude at 2.5 MHz.

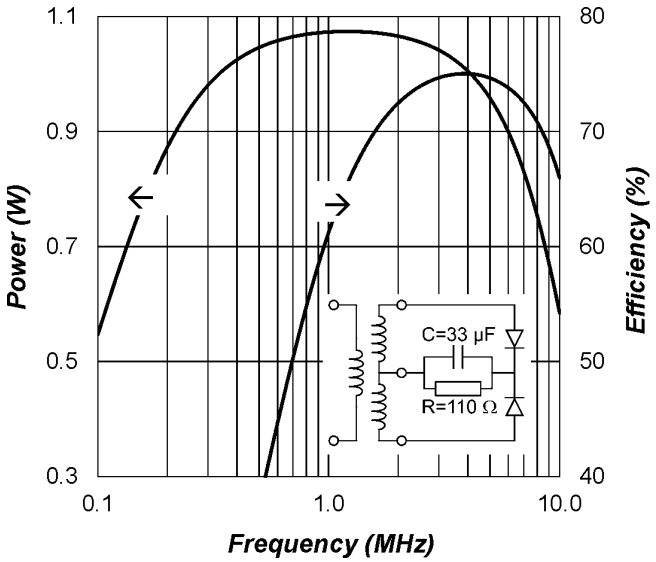

Fig. 20: Transmission efficiency and transmitted power of transformer (c) calculated for primary voltage amplitude of 15 V. Power is supplied to the gate driver by means of full-wave rectification (inset).

VI. Conclusions

The inevitable merging of economic and ecologic interests requires smart and power-efficient infrastructure with distributed electronic sensors and controllers being locally integrated with power electronics. Transformers are key components to link these functional blocks as they combine power transmission capability with galvanic isolation. To this end, the innovations presented here address the design and the manufacture of space-saving, up-to-100 W transformers squeezed into otherwise unused space inside multilayer circuit boards. The easy-to-use, accurate design process and the low-temperature-ceramic cofiring (LTCC) technology for manufacturing embedded components in mixed dielectric-magnetic ceramic multilayer boards have both been described for the first time. Exam-

ples from light-emitting diodes (LED) and electric vehicle (EV) power inverters demonstrate the efficiency and the reliability of the design process and the manufacturing technology. Casting electromagnetic theory into few analytical equations and applying these to a reduced set of geometric device parameters implicates a number of benefits over lengthy finite element approaches: Performance predictions including magnetizing inductances, leakage inductances or power transmission are available within minutes; the device geometry and the choice of materials, e.g. the ferrite for the magnetic core, can be modified and driven toward their optimum similarly fast. Although the resulting designs can be manufactured by a number of alternative technologies, the applications presented, call for high-end solutions either owing to high-temperature or high-frequency conditions or both. The combination of magnetic and dielectric ceramics in a single, cofired circuit board has now been successfully achieved with two alternative approaches: Interposing a sinter-stop between the two materials or matching their sintering characteristics. The first technology avoids the rigid connection between ferrite and dielectric; therefore a wide class of ferrites can be used. The second technology produces a truly monolithic board for places with high vibrational exposure, however, at the expense of sophisticated material engineering and limited choice of matching materials. Finally, both solutions not only permit the fabrication of flat, thermally robust transformers, but also their integration into an otherwise conventional dielectric ceramic multilayer board.

Acknowledgment

This work was supported by the German Federal Ministry of Education and Research (BMBF) under grants NIKOL (03X4503B, 03X4503F), ALFERMO (16N10663, 16N10664, 16N10668), and KAIROS (16N11657, 16N11658). The authors thank R. Karmazin and R. Männer for developing a low-temperature-firable Mn-Zn ferrite material and a suitable process for cofiring with commercial dielectric LTCC tapes at Siemens AG. Further thanks are addressed to B. Capraro and S. Barth of the Fraunhofer IKTS for casting the ferrite tapes. Likewise, the preparation, cofiring, and characterization of numerous multilayer types by H. Naghib-zadeh and dilatometer measurements by R. Schadrack are acknowledged by the Federal Institute for Materials Research and Testing.

References

1 Jiang, H., Wang, Y., Yeh, J.L.A., Tien, N.C.: On-chip spiral inductors suspended over deep copper-lined cavities, *IEEE Trans. Microwave Theory Techn.*, **48**, 2415 – 2423, (2000).

2 Zou, J., Liu, C., Trainor, D.R., Chen, J., Schutt-Ainé, J.E., Chapman, P.L.: Development of three-dimensional inductors using plastic deformation magnetic assembly (PDMA), *IEEE Trans. Microwave Theory Techn.*, **51**, 1067 – 1075, (2003).

3 Rais-Zadeh, M., Laskar, J., Ayazi, F.: High performance inductors on CMOS-grade trenched silicon substrate, *IEEE Trans. Comp. Pack. Technol.*, **31**, 126 – 134, (2008).

4 Karmazin, R., Dernovsek, O., Ilkov, N., Wersing, W., Roosen, A., Hagymasi, M.: New LTCC-hexaferrites by using reaction bonded glass ceramics, *J. Eur. Ceram. Soc.*, **25**, 2029 – 2032, (2005).

5 Matters-Kammerer, M., Mackens, U., Reimann, K., Pietig, R., Hennings, D., Schreinemacher, B., Mauczok, R., Gruhlke, S., Martiny, C.: Material properties and RF applications of high k and ferrite LTCC ceramics, *Microelectr. Relia.*, **46**, 134 – 143, (2006).

6 Macrelli, E., Romani, A., Wang, N., Roy, S., Hayes, M., Paganelli, R.P., Tartagni, M.: Design and fabrication of a 29μH bond wire micro-transformer with LTCC magnetic core on silicon for energy harvesting applications, *Proc. Eng.*, **87**, 1557 – 1560, (2014).

7 Lahti, M., Lantto, V., Leppävuori, S.: Planar inductors on an LTCC substrate realized by gravure-offset-printing technique, *IEEE Trans. Comp. Pack. Technol.*, **23**, 606 – 610, (2000).

8 Dick, C.P., Hirschmann, D., Plum, T., Knobloch, D., De Doncker, R.W.: Novel high frequency transformer configurations – amorphous metal vs. ferrites. In: *Proc. 39th Annual IEEE Power Electronics Specialists Conf. (PESC)*, 4264 – 4269. Technical University of Athens, Rhodes, Greece, (2008).

9 Ludwig, M., Duffy, M., O'Donnell, T., McCloskey, T.P., Ó Mathùna, S.C.: PCB integrated inductors for low power DC/DC converter, *IEEE Trans. Power Electr.*, **18**, 937 – 945, (2003).

10 Waffenschmidt, E.: Design and application of thin, planar magnetic components for embedded passive integrated circuits. In: *Proc. 35th Annual IEEE Power Electronics Specialists Conf. (PESC)*, 4546 – 4552. Aachen, Germany, (2004).

11 Tada, N., Tabuchi, T., Ikezaki, H.: Inductor part and method of producing the same. European Patent Application EP 1 367 611 A1, (2002).

12 Barth, S., Bechtold, F., Müller, E., Mürbe, J., Töpfer, J.: Low sintering Ni-Cu-Zn ferrite tapes for LTCC integrated inductors. In: *Proc. 1st IMAPS/ACerS Int. Conf. Ex. Ceramic Interconnect and Ceramic Microsystems Technol. (CICMT)*. Baltimore, USA, (2005).

13 Hahn, R., Sommer, G., Dörr, I., Schwerzel, S., Reichl, H.: Design of integrated inductances based on ferromagnetic LTCC layers, *Ad. Microelectr.*, **33**, 8 – 16, (2006).

14 Lim, M.H., Liang, Z., van Wyk, J.D.: Low profile integratable inductor fabricated based on LTCC technology for microprocessor power delivery applications, *IEEE Trans. Comp. Pack. Technol.*, **30**, 170 – 177, (2007).

15 Lim, M.H., van Wyk, J.D., Lee, F.C., Ngo, K.D.T.: A class of ceramic-based chip inductors for hybrid integration in power supplies, *IEEE Trans. Power Electr.*, **23**, 1556 – 1564, (2008).

16 Slater, C., Maeder, T., Ryser, P.: Fabrication and test of high-temperature ceramic transformer, *Solid State Phenomena*, **216**, 233 – 238, (2014).

17 Lin, Y.-C., Gabler, F., Tsai, Y.-C., Tanaka, S., Gessner, T., Esashi, M.: LTCC-based three dimensional inductors with nano-ferrite embedded core for on-chip tunable RF systems. In: *Proc. 17th Int. Conf. on Solid-State Sensors, Actuators and Microsystems*, University of Barcelona, Barcelona, Spain, (2013).

18 Maric, A., Radosavljevic, G., Blaz, N., Zivanov, L.: Fine tuning of 3D LTCC inductor properties using combination of different ferrite and dielectric tapes, *Int. J. Appl. Ceram. Technol.*, **12**, 1034 – 1044, (2015).

19 Jao, J.C., Li, P., Wang, S.F.: Characterization of inductor with Ni-Zn-Cu ferrite embedded in B_2O_3-SiO_2 glass, *Jpn. J. Appl. Phys.,* **46**, 5792 – 5796, (2007).

20 Lipkes, Z.: Core and coil structure and method of making the same. US patent 5 945 902, (1999).

21 Sato, T., Yokoyama, H., Yamasawa, K., Toya, K., Kobayashi, S., Minamisawa, T.: Multilayered transformer utilizing mn-zn

ferrite and its application to a forward-type DC-DC converter, *Electr. Eng. Jpn.*, **135**, 1 – 8, (2001).

22 Yu, Q., Wang, H., Geng, Y., Liu, Z.: Research of LTCC NiCuZn transformer prototype. In: *Proc. 6th World Congr. Intelligent Control and Automation*, 5272 – 5276. Dalian University of Technology, Dalian, China, (2006).

23 Waffenschmidt, E., Jacobs, J.: Planar resonant multi-output transformer for printed circuit board integration. In: *Proc. 39th Annual Power Electronics Specialists Conf. (PESC)*, 4222 – 4228. Technical University of Athens, Rhodes, Greece, (2008).

24 Abel, D.A.: Multi-layer transformer apparatus and method. US patent 6 198 374 B1, (2001).

25 Wahlers, R.L., Huang, C.Y.D., Heinz, M.R., Feingold, A.H., Bielawski, J., Slama, G.: Low profile LTCC transformers. In: *Proc. 2002 Int. Symp. Microelectronics*, 76 – 80. Denver, Colorado, (2002).

26 Slama, G.: Low-temp co-fired magnetic tape yields high benefits, *Power Electr. Technol.*, **1**, 30 – 34, (2003).

27 Lebourgeois, R., Laboure, E., Lembeye, Y., Ferrieux, J.-P.: LTCC magnetic components for high density power converter, *AIP Advances*, **8**, 047901, (2018).

28 Matz, R.: Integration technologies for ferrites and power inductors in ceramic circuit boards. In: *Ceramic Integration and Joining Technologies*, 233 – 265. Ed. M. Singh, T. Ohji, R. Asthana, S. Mathur. John Wiley & Sons, New York, (2011).

29 Küpfmüller, K.: Introduction to Theoretical Electrical Engineering, in German, 10th edition, Springer, Berlin, (1973).

30 Matz, R., Götsch, D., Gossner, T., Karmazin, R., Männer, R., Siessegger, B.: Power inductors in ceramic multilayer circuit boards, *J. Microelec. Elec. Pack.*, **5**, 161 – 168, (2008).

31 Pozar, D.M.: Microwave Engineering, 2nd edition. John Wiley & Sons, New York, 211, (1998).

32 Matz, R., Götsch, D., Karmazin, R., Männer, R.: Ceramic multilayer integration of power electronic inductors, *J. Ferroelec.*, **387**, 77 – 84, (2009).

33 Ferrite type Fi328 by Sumida Corp., Tokyo, Japan; or ferrite type N27 by TDK Europe GmbH, Munich, Germany.

34 Matz, R., Götsch, D., Karmazin, R., Männer, R., Siessegger, B.: Low temperature cofirable MnZn ferrite for power electronic applications, *J. Electroceram.*, **22**, 209 – 215, (2009).

35 Ferrite type 3F4. In: Soft ferrites and accessories, data handbook. Ferroxcube International Holding B.V.

36 Nakamura, T., Okano, Y.: Low temperature sintered ni-zn-cu ferrite, *J. Phys. IV*, **7 C1**, 91 – 92, (1997).

37 Yasuda, K., Mochizuki, Y., Takaya, M.: Multilayer ferrite chip component for growth of microelectronics. In: *Proc. 8th Int. Conf. Ferrites ICF8*, 1162 – 1164. Kyoto, Japan, (2000).

38 Mürbe, J., Töpfer, J.: Low temperature sintering of sub-stoichiometric ni-cu-zn ferrites: shrinkage, microstructure and permeability, *J. Magn. Magn. Mater.*, **324**, 578 – 583, (2012).

39 Mürbe, J., Töpfer, J.: Ni-Cu-Zn ferrites for low temperature firing: II. Effects of powder morphology and Bi_2O_3 addition on microstructure and permeability, *J. Electroceram.*, **16**, 199 – 205, (2006).

40 Jeong, J., Han, Y.H., Moon, B.: Effects of Bi_2O_3 addition on the microstructure and electromagnetic properties of NiCuZn ferrites, *J. Mater. Sci.*, **15**, 303 – 306, (2004).

41 Rabe, T., Naghib-zadeh, H., Glitzky, C., Töpfer, J.: Integration of Ni-Cu-Zn ferrite in low temperature Co-fired ceramics LTCC modules, *Int. J. Appl. Ceram. Technol.*, **9**, 18 – 28, (2012).

42 Hesse, J., Naghib-zadeh, H., Rabe, T., Töpfer, J.: Integration of additive-free Ni-Cu-Zn ferrite layers into LTCC multilayer modules, *J. Eur. Ceram. Soc.*, **36**, 1931 – 1937, (2016).

43 Naghib-zadeh, H., Hesse, J., Reimann, T., Töpfer, J., Rabe, T.: Effect of oxygen partial pressure on co-firing behavior and magnetic properties of LTCC modules with integrated ni-cu-zn ferrite layers, *J. Electroceram*., **37**, 100 – 109, (2016).

44 Priven, A.: General method for calculating the properties of oxide glasses and glass forming melts from their composition and temperature, *Glass Techn.*, **45**, 244 – 249, (2004).

45 Naghib-zadeh, H., Rabe, T., Karmazin, R.: Integration of MnZn-ferrite tapes in LTCC multilayer, *J. Electroceram.*, **31**, 88 – 95, (2013).

46 Glitzky, C., Rabe, T., Eberstein, M., Schiller, W., Töpfer, J., Barth, S., Kipka, A.: LTCC-modules with integrated ferrite layers – strategies for material development and co-sintering, *J. Microelec. Elec. Pack.*, **6**, 1 – 5, (2009).

47 Rabe, T., Glitzky, C., Naghib-Zadeh, H., Oder, G., Eberstein, M., Töpfer, J.: Silver in LTCC – Interfacial reactions, transport processes and influence on ceramic properties. In: *Proc. 5th CICMT*, 85 – 93, Denver, Colorado. (2009).

48 Provided by Tanaka Paper Industry Corp., 1426 Tono-Machi, Mino-City, Japan 501 – 3742 (2013).

49 Bartsch, H., Albrecht, A., Hoffmann, M., Müller, J.: Microforming process for embossing of LTCC tapes, *J. Micromech. Microeng.*, **22**, 015004, (2012).

50 Bartsch, H., Geiling, T., Müller, J.: An LTCC low-loss inductive proximity sensor for harsh environments, *Sens. Act. A*, **175**, 28 – 34, (2012).

51 Ziesche, S., Ihle, M., Eberstein, M.: High current conductors in LTCC. In: *Proc. IMAPS/ACerS 8th Int. Conf. Ex. Ceramic Interconnect and Ceramic Microsystems Technol. (CICMT)*. Erfurt, Germany, (2012).

52 Welker, T., Gutzeit, N., Müller, J.: Enhanced heat spreading in LTCC packages utilizing thick silver tape in the co-fire process. In: *Proc. 21st Eur. Microelectronics Packaging Conf. (EMPC)*. Warsaw Technical University, Warsaw, Poland, (2017).

53 Ihle, M., Ziesche, S., Gierth, P.: LTCC technology for active eddy current turbocharger speed sensors. In: *Proc. 21st Eur. Microelectronics Packaging Conf. (EMPC).* Warsaw Technical University, Warsaw, Poland, (2017).